

Net Community Production and Inorganic Carbon Cycling in the Irminger Sea

Meg F Yoder¹, Hilary Ilana Palevsky¹, and Kristen E Fogaren²

¹Boston College, Department of Earth and Environmental Sciences

²Boston College

February 23, 2024

Abstract

The subpolar North Atlantic plays an outsized role in the atmosphere-to-ocean carbon sink. The central Irminger Sea is home to well-documented deep winter convection and high phytoplankton production, which drive strong seasonal and interannual variability in regional carbon cycling. We use observational data from moored carbonate system chemistry sensors and annual turn-around cruise samples at the Ocean Observatories Initiative's Global Irminger Sea Array to construct a near-continuous time series of mixed layer dissolved inorganic carbon (DIC), pCO₂, and total alkalinity from summer 2015 to summer 2022. We use these carbonate system chemistry time series to deconvolve the physical and biological drivers of surface ocean carbon cycling in this region on seasonal, annual, and interannual time scales. We find high annual net community production within the seasonally-varying mixed layer, averaging 9.7 ± 1.7 mol m⁻² yr⁻¹ with high interannual variability (range of 6.0 to 13.7 mol m⁻² yr⁻¹). The highest daily net community production rates occur during the late winter and early spring, prior to the observed high chlorophyll concentrations associated with the spring phytoplankton bloom. As a result, the winter and early spring play a much larger role in biological carbon export from the mixed layer than traditionally thought.

Hosted file

AGU_Manuscript_Yoder_final.docx available at <https://authorea.com/users/540400/articles/717817-net-community-production-and-inorganic-carbon-cycling-in-the-irminger-sea>

Hosted file

AGU_SuppInfo_Yoder_final.docx available at <https://authorea.com/users/540400/articles/717817-net-community-production-and-inorganic-carbon-cycling-in-the-irminger-sea>

1
2
3
4
5
6
7
8
9
10
11
12
13

Net Community Production and Inorganic Carbon Cycling in the Irminger Sea

M. F. Yoder¹, H. I. Palevsky¹, and K. E. Fogaren¹

¹Boston College, Department of Earth and Environmental Science.

Corresponding author: Meg Yoder (yoderma@bc.edu)

Key Points:

- We present the first multi-year, near-daily mixed layer dissolved inorganic carbon time series in the Irminger Sea
- Annual net community production within the seasonally varying mixed layer is high ($9.7 \pm 1.7 \text{ mol m}^{-2} \text{ yr}^{-1}$) and has large interannual variability
- The greatest rates of inorganic carbon removal from the mixed layer via photosynthesis take place prior to mixed layer shoaling

14 Abstract

15 The subpolar North Atlantic plays an outsized role in the atmosphere-to-ocean carbon sink. The
16 central Irminger Sea is home to well-documented deep winter convection and high
17 phytoplankton production, which drive strong seasonal and interannual variability in regional
18 carbon cycling. We use observational data from moored carbonate system chemistry sensors and
19 annual turn-around cruise samples at the Ocean Observatories Initiative's Global Irminger Sea
20 Array to construct a near-continuous time series of mixed layer dissolved inorganic carbon
21 (DIC), $p\text{CO}_2$, and total alkalinity from summer 2015 to summer 2022. We use these carbonate
22 system chemistry time series to deconvolve the physical and biological drivers of surface ocean
23 carbon cycling in this region on seasonal, annual, and interannual time scales. We find high
24 annual net community production within the seasonally-varying mixed layer, averaging 9.7 ± 1.7
25 $\text{mol m}^{-2} \text{yr}^{-1}$ with high interannual variability (range of 6.0 to $13.7 \text{ mol m}^{-2} \text{yr}^{-1}$). The highest
26 daily net community production rates occur during the late winter and early spring, prior to the
27 observed high chlorophyll concentrations associated with the spring phytoplankton bloom. As a
28 result, the winter and early spring play a much larger role in biological carbon export from the
29 mixed layer than traditionally thought.

30 Plain Language Summary

31 The subpolar North Atlantic takes in more carbon from the atmosphere than other areas of the
32 ocean relative to its size. This is partially caused by photosynthesis in the surface ocean, which
33 turns inorganic carbon into organic carbon that is transported into the deep ocean, a process
34 known as the biological carbon pump. Using measurements from sensors on moorings in the
35 Irminger Sea, we construct a seven-year time series of the different parts of the inorganic carbon
36 system. Using these, we separate out the forces that impact how much inorganic carbon has the
37 potential to be exchanged with the atmosphere. We find that biological processes remove
38 inorganic carbon from the surface ocean in the spring, summer, and early fall, while in the winter
39 the surface ocean gets deeper and encompasses waters from below that have higher carbon
40 content. The total amount of inorganic carbon removed from the surface ocean each year by
41 biological process is extremely high in the Irminger Sea compared to other global ocean regions.
42 This research highlights the importance of long-term, full year measurements to understand
43 carbon cycle dynamics.

44

45

46

47

48 **1 Introduction**

49 The ocean acts as a key sink in the global carbon cycle, absorbing carbon from the atmosphere at
50 its surface and then storing it in the deep ocean. Different biological and physical factors work in
51 tandem to drive this uptake. The biological carbon pump transports organic carbon produced via
52 photosynthesis into the deep ocean, causing a decrease in surface ocean $p\text{CO}_2$ that results in
53 carbon dioxide moving from atmosphere to ocean (DeVries, 2022; Volk & Hoffert, 1985).
54 Globally, the biological carbon pump moves approximately 10 PgC yr^{-1} into the ocean interior
55 and is the main contributor to the 40-fold difference between the ocean and atmosphere carbon
56 reservoirs (Caldera et al., 2018; Friedlingstein et al., 2022; Siegel et al., 2023). The North
57 Atlantic accounts for a disproportionately large share of this global export relative to its size,
58 with estimates ranging from 0.55 to 1.94 PgC yr^{-1} (average 1.27 PgC yr^{-1} ; Sanders et al., 2014).
59 While extensive study has taken place in the North Atlantic on the myriad of pathways
60 contributing to the region's biological carbon export, there is still high uncertainty in total flux
61 values and the underlying mechanistic controls (Sanders et al., 2014).

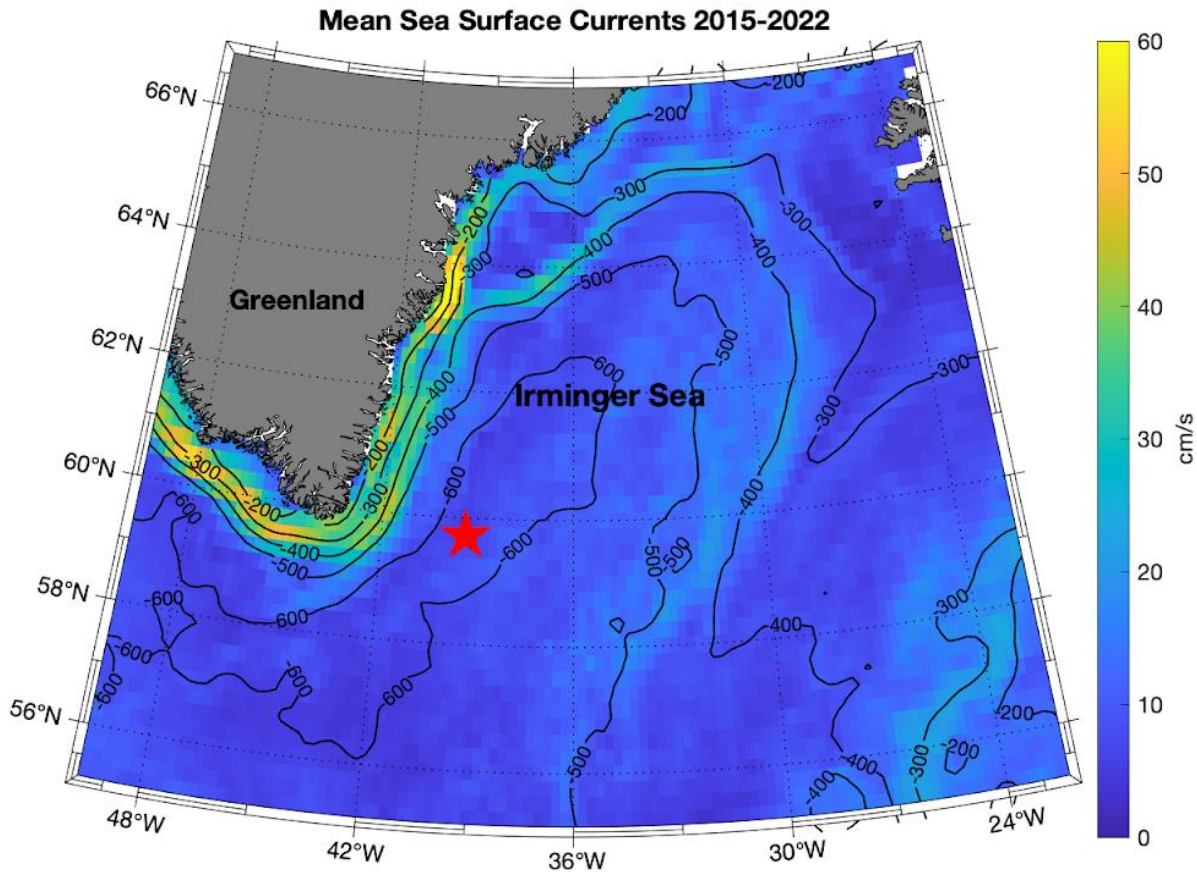
62 Organic carbon meanders on its path from the surface to the deep ocean. It can be repeatedly
63 aggregated, disaggregated, consumed, and respired by different classes of organisms, and is
64 transported via sinking of particles, physical injection of high organic carbon waters, and vertical
65 migration of heterotrophic grazers (Boyd, 2015; Boyd et al., 2019; Huang et al., 2022; Siegel et
66 al., 2023; Stemmann & Boss, 2012). While known as the biological carbon pump, the physical
67 processes involved in removing organic carbon from the surface cannot be siloed. In the North
68 Atlantic, large spring phytoplankton blooms are thought to be the primary driver of high carbon
69 export (Martin et al., 2011), however physical processes like deep convection have the potential
70 to counterbalance this export by entraining previously exported carbon (Kortzinger et al., 2008;
71 Palevsky & Nicholson, 2018; Quay et al., 2012, 2020). These dynamics are especially strong in
72 the subpolar North Atlantic, which contains the deepest winter convection on Earth (de Jong et
73 al., 2018; de Jong & de Steur, 2016; Holte et al., 2017) and high primary productivity (Boss &
74 Behrenfeld, 2010; Henson et al., 2006, 2009).

75 To investigate the intertwined roles of biology and physics on carbon export, we use carbonate
76 chemistry system measurements of dissolved inorganic carbon (DIC) and total alkalinity (TA)
77 which provide mechanistically agnostic tracers of the removal and addition of carbon from the
78 surface ocean. Net community production (NCP) is a measure of the net biologically produced
79 organic carbon in the upper ocean. It can be determined using inorganic carbon measurements
80 and when integrated throughout the year represents the biological pump on an annual basis
81 (ANCP, Emerson, 2014). Marine carbon cycling has been studied around the globe by making
82 inorganic carbon system measurements at regular intervals throughout the year since the early
83 1980's (Bates et al., 2014). However, these historic discrete shipboard measurements have not
84 provided adequate temporal resolution to constrain the full seasonal and interannual variability
85 influencing ANCP using carbonate chemistry (Bates et al., 2014; Racapé et al., 2013).

86 Technological advances since the turn of the century have increased observational capacity,
87 providing high frequency time series measurements (more than once a day) for a number of
88 chemical and physical parameters on both stationary mooring arrays and mobile floats and
89 gliders. These have enabled the construction of DIC and TA mass balance budgets in the
90 Northeast Atlantic, North Pacific, and Southern Ocean, and the subsequent disentanglement of
91 biological and physical forcing on carbon cycling and quantification of annual net community
92 production (Fassbender et al., 2016, 2017; Haskell et al., 2020; Huang et al., 2022; Knor et al.,
93 2023; Kortzinger et al., 2008; Sauvé et al., 2023; Yang et al., 2021).

94 The Irminger Sea is an area of particular interest within the North Atlantic and is the location of
95 the Global Irminger Sea Array (operated by the NSF's Ocean Observatories Initiative, OOI). The
96 location was selected in order to provide sustained atmospheric, physical, and biogeochemical
97 observations at a high latitude site, with a focus on the critical influences that affect the global
98 ocean-atmosphere system (Fig 1., Ocean Observatories Initiative Science Prospectus, 2007;
99 Smith et al., 2018). Fast moving currents bring water southward along the eastern coast of
100 Greenland, and warm waters move northward along the eastern boundary as part of the North
101 Atlantic current, forming the central Irminger Gyre where the array is located (de Jong et al.,
102 2018). A 19-year time series (2002-2020) using OOI and nearby mooring data finds extreme
103 variability in the depth of winter convection (285-1480 m, de Jong et al., 2024). Prior work in the
104 region has used oxygen production as a tracer of photosynthesis and respiration (Palevsky &
105 Nicholson, 2018) and the carbonate system seasonal cycle has been generally characterized
106 (Bates et al., 2014; Racapé et al., 2013). As with many sites, there has not been sufficient data in
107 the Irminger Sea to resolve full year-round net community production until now. Understanding
108 the controls on the biological pump in subregions like the Irminger Sea contributes to our overall
109 understanding of the North Atlantic's current carbon export and the potential changes it may
110 undergo as a result of climate change, including changes in primary productivity, surface and
111 deep ocean respiration, and physical transport. Here, we use seven years of high temporal
112 frequency mooring data from the OOI Irminger Sea Array to provide the longest near-continuous
113 daily carbonate chemistry dataset to date in this region. We leverage these data to determine the
114 biological and physical forcing on carbon cycling and quantify net community production over
115 seasonal, annual, and interannual time scales in the subpolar North Atlantic.

116



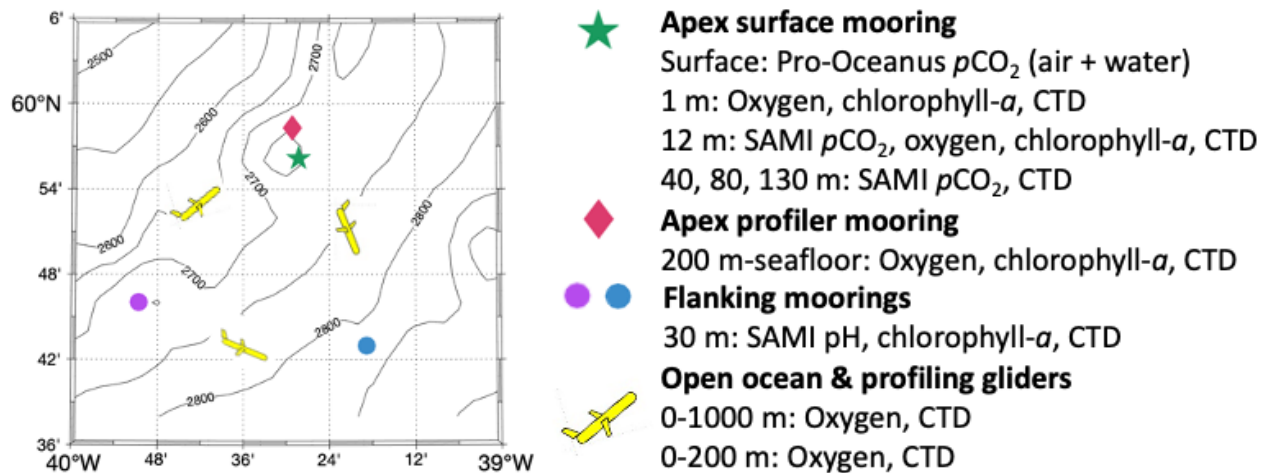
117

118 **Figure 1.** Map showing the Irminger Sea and location of Ocean Observatories Initiative Global
 119 Irminger Array (red star). The colored shading is the mean sea surface currents and the black
 120 contours are the mean sea surface height in millimeters for 2015-2022. Data are from E.U.
 121 Copernicus Marine Service Information, <https://doi.org/10.48670/moi-00148>.

122 2 Data

123 2.1 Ocean Observatories Initiative Global Irminger Sea Array

124 The Ocean Observatories Initiative (OOI) is a 25-year, NSF funded program that began
 125 collecting data in 2014, after nearly a decade of proposals and planning (Cowles et al., 2010;
 126 Isern & Clark, 2003; Smith et al., 2018). Our primary data source is the OOI Global Irminger
 127 Sea Array, which is comprised of 4 moorings, triangularly arranged and spaced approximately
 128 20 km apart, and profiling and open ocean gliders (Fig. 2). Repeat hydrography at the mooring
 129 locations is also available from annual turn-around cruises. Our analysis focuses on the pH and
 130 $p\text{CO}_2$ sensors, all of which are located in the upper 130m of the water column, as well as their
 131 co-located CTDs.



132

133 **Figure 2.** Schematic showing locations of the autonomous biogeochemical sensors and co-
 134 located CTDs on the OOI Irminger Array used in this analysis. Contour lines on the map show
 135 local bathymetry (m).

136 All carbonate system sensors, except at the surface, are Submersible Autonomous Moored
 137 Instruments (SAMI) made by Sunburst Sensors; both the pH and $p\text{CO}_2$ versions utilize
 138 spectrophotometry and a pH sensitive indicator dye (Álvarez et al., 2020; Lai et al., 2018). The
 139 surface $p\text{CO}_2$ sensor is a Pro-Oceanus CO_2 -Pro, which operates above and below the water,
 140 making air and seawater measurements using infrared detection (Jiang et al., 2014). The pH and
 141 $p\text{CO}_2$ sensors below the surface make a measurement every 2 hours and the surface $p\text{CO}_2$ sensor
 142 makes a measurement every hour, though occasionally measurements are further apart due to
 143 battery limitations. Shallow sensors (pH sensors at 20m & 30m; $p\text{CO}_2$ sensors at 0m, 12m, &
 144 40m) are in the mixed layer for the majority of the annual cycle, while deeper sensors (pH 100m,
 145 $p\text{CO}_2$ 80m & 130m) are only in the mixed layer in the winter. The 20m and 100m pH sensors
 146 have very little usable data and have been excluded from this analysis.

147 pH and $p\text{CO}_2$ data were quality controlled using gross range and spike tests based on Quality
148 Assurance / Quality Control of Real Time Oceanographic Data (QARTOD) recommendations,
149 followed by a moving median filter (Palevsky et al., 2023; U.S. Integrated Ocean Observing
150 System, 2020; Table S1). We also remove data deemed suspect based on OOI operational
151 annotations (for further detail, see the OOI Biogeochemical Sensor Data Best Practices and User
152 Guide; Palevsky et al., 2023). The fixed asset data within the mixed layer for pH, $p\text{CO}_2$,
153 temperature, salinity, and pressure are at times sparse, with different depths and locations
154 available across the time series (Fig. S1 and S2). This sparsity is primarily due to infrastructure
155 and instrument failures, which tend to occur during the late winter when seas are extremely
156 rough and power becomes limited due to low sun angle. As a result, we have opted to combine
157 all carbonate system sensor data within the mixed layer in order to create the most complete time
158 series possible. Previous work has shown that the horizontal spatial variability is low enough to
159 analyze sensors across the array as one data stream (de Jong et al., 2018; Palevsky & Nicholson,
160 2018).

161 Beyond the upper ocean carbonate system chemistry and CTD sensors, we use calibrated oxygen
162 data from the wire-following profiler on the Apex profiler mooring (200-2000m, one cycle every
163 20 hours) and gliders (0-200m and 0-1000m, varying temporal coverage). These are corrected
164 using repeated stable deep oxygen measurements on the 3.1θ isotherm (~1800-2000m), based on
165 the approach previous applied at the Irminger Sea Array by Palevsky & Nicholson (2018). These
166 oxygen data are used for carbonate system predictions below the mixed layer using the
167 CONTENT model (Bittig et al., 2018). We also use chlorophyll-*a* data from Sea-Bird/WETLabs
168 fluorimeters deployed on the OOI moorings at 1m, 12m, and 30m during periods they are within
169 the mixed layer. These data are presented for qualitative rather than quantitative interpretation, as
170 end-user quality control and calibration of the fluorometer data are beyond the scope of this
171 work.

172 2.2 Cruise Data

173 During the turn-around cruise each summer, discrete dissolved inorganic carbon (DIC), pH, and
174 total alkalinity (TA) samples are collected at depths corresponding to the deployment depths of
175 moored pH and $p\text{CO}_2$ sensors (Palevsky et al., 2023). In addition to the discrete samples
176 routinely collected and analyzed by the OOI program, we collected and analyzed additional DIC
177 and TA samples from the 2018 and 2019 turn-around cruises (Palevsky et al. 2023b). Quality
178 control of the discrete DIC, pH, and TA samples provided by the OOI program identified
179 inconsistencies among these three carbonate system chemistry variables that indicate data quality
180 issues with a subset of the TA samples. We therefore rely primarily on directly-measured
181 discrete DIC data rather than on other measured or calculated carbonate chemistry variables in
182 calibrating and validating the sensor-based time series. Our analysis also uses calibrated salinity,
183 temperature, and oxygen depth profiles from sensors on the CTD rosette (Fogaren et al., 2023;
184 McRaven, 2022a-d).

185 **3 Methods**

186 3.1 Carbonate System Time Series

187 We synthesize the fixed mooring assets to construct a near-continuous mixed layer carbonate
188 system chemistry time series over the seven year period from summer 2015 through summer
189 2022. The mixed layer depth fluctuates significantly throughout the year, which results in the
190 carbonate system sensors below the nominal 12m sensor alternating being in the mixed layer and
191 below it, depending on their deployment depths and the current depth of mixing. For our mixed
192 layer time series, we use only sensors deployed at nominally 40m and shallower; the process
193 used to determine when sensors are in the mixed layer is described in Section 2 of the
194 Supplementary Information (Fig. S3).

195 3.1.1 Total Alkalinity

196 Due to the close co-varying relationship between total alkalinity (TA) and salinity, regressions
197 between the two have long been used to estimate total alkalinity for carbonate system
198 calculations (Millero et al., 1998), with other variables having been incorporated in more recent
199 work. We use the Locally Interpolated Alkalinity Regression (LIAR) model to predict TA from
200 mixed layer sensor data, using temperature, salinity, and location as predictors (Carter et al.,
201 2018).

202 3.1.2 Dissolved Inorganic Carbon

203 For each $p\text{CO}_2$ and pH sensor, DIC was calculated from daily averages of the sensor
204 measurements and estimated total alkalinity (described above) using CO2SYS, with temperature,
205 pressure, and salinity from co-located CTDs (Lewis & Wallace, 1998; Orr et al., 2018; van
206 Heuven et al. 2011). Silicate and phosphate are also calculation inputs as they contribute to the
207 acid-base system, however DIC outputs are very insensitive to these inputs ($< 1 \mu\text{mol kg}^{-1}$
208 difference calculated using the minimum and maximum values ever recorded in the region). As a
209 result, we use mean nutrient values from regional GLODAPv2_2021 data (Lauvset et al., 2021;
210 Olsen et al., 2016). We used the dissociation constants of Lueker et al. (2000), the KSO_4 constant
211 of Dickson (1990), and the total boron constant of Uppström (1974). Days with fewer than 2
212 measurements of $p\text{CO}_2$ or pH values are excluded. There are several short gaps in the time series
213 where no carbonate system data is available. In the later part of the time series (summer 2018 -
214 summer 2022) we fill these gaps using DIC predicted using CONTENT from the calibrated 1m
215 and 12m moored oxygen sensors, with the longest gap being about 2 months in summer 2019
216 and all others being less than two weeks (Fig. S4).

217

218

219 3.1.3 Calibrating the DIC time series

220 Our use of a multitude of carbonate system chemistry sensors requires confirmation that these
221 sensors are accurately measuring our parameters of interest. Once calibrated, the DIC time series
222 calculated from individual sensors in the mixed layer match well with validation data from
223 deeper moored assets as well as discrete cruise samples. The SAMI $p\text{CO}_2$ sensors show
224 significant offsets from one another and from the Pro-Oceanus $p\text{CO}_2$ sensor during some
225 deployments, but follow the same seasonal, weekly, and daily patterns when in the mixed layer
226 (Fig. S5a). The SAMI pH sensors also show offsets, though much less substantial. The offsets
227 between the SAMI sensors are not consistent annually, and there is no offset seen in the
228 temperature data of the co-located CTDs, which indicates a known sensor calibration issue that
229 require correction rather than a true signal (DeGrandpre et al., 2004; Kortzinger et al., 2008). The
230 shallower $p\text{CO}_2$ and pH sensors (12-40m) used in the mixed layer time series are generally
231 within a steep thermocline during turn-around cruises in summer, precluding aligning the
232 moored sensor data with the discrete samples collected from co-located CTD casts as a
233 calibration approach itself.

234 Unlike the SAMI sensors, when the Pro-Oceanus surface $p\text{CO}_2$ sensor measures for the entire
235 deployment, the newly deployed sensor matches the previously deployed sensor while both are
236 operational, which instills confidence in the accuracy of the surface Pro-Oceanus (summer 2020
237 and 2021, Fig. S1). The Pro-Oceanus, however, fails after only weeks to months in five out of
238 the seven deployments used in this analysis. In order to create a complete mixed layer time
239 series, we leverage the strengths of both carbonate chemistry sensor systems on the array,
240 namely the longevity of the SAMI sensors and the accuracy of the Pro-Oceanus. We correct for
241 offsets in the DIC time series calculated from the shallow (12-40m) SAMI pH and $p\text{CO}_2$ sensors
242 by aligning them with the available DIC time series calculated from the Pro-Oceanus, after
243 which we average all DIC data in the mixed layer (Supplementary Information Section 4, Fig.
244 S5).

245 While we do not use the 80m and 130m $p\text{CO}_2$ sensor data as part of our mixed layer time series,
246 they provide a useful check on our calibration process. The final mixed layer DIC time series
247 shows good agreement with these deeper sensor DIC data, calibrated using predicted DIC from
248 turn-around cruise CTD dissolved oxygen measurements, once they reenter the mixed layer (Fig.
249 S5c, Bittig et al., 2018; Palevsky et al., 2023b). This agreement with the independently calibrated
250 deep sensors, as well as with the available discrete cruise data points, further instills confidence
251 in the choice to align the 12-40m DIC time series with the DIC time series from the Pro-Oceanus
252 (Fig. S5c). A detailed explanation of the calibration processes can be found in Section 4 of the
253 Supplementary Information.

254

255

256 3.1.4 $p\text{CO}_2$

257 We fill in the gaps in the surface $p\text{CO}_2$ record directly measured by the Pro-Oceanus using $p\text{CO}_2$
 258 calculated from the mixed layer DIC time series, mixed layer estimated total alkalinity, salinity
 259 at 30m, and the fifth generation European Centre for Medium-Range Weather Forecasts
 260 atmospheric reanalysis (ERA5) sea surface temperature (Fig. S8, Hersbach et al., 2020). Salinity
 261 at 30m is used because there are frequent gaps in the surface $p\text{CO}_2$ record due to surface mooring
 262 platform failures, which also affected the co-located CTDs.

263 3.2 Mixed Layer Budget

264 Seasonal changes in the observed mixed layer DIC concentration are driven by physical
 265 transport, gas exchange, evaporation and precipitation, and biological processes, namely net
 266 community production and calcium carbonate production and dissolution (eq.1, Fassbender et
 267 al., 2016, 2017; Haskell et al., 2020; Kortzinger et al., 2008; Palevsky & Quay, 2017; Yang et
 268 al., 2021). Changes in total alkalinity are driven by the same processes as DIC, with the
 269 exception of gas exchange (eq. 2). The time rate of change terms for each tracer (left hand side of
 270 eq. 1 and 2, respectively) are determined from the DIC and TA time series data. Observational
 271 data allows us to calculate the non-biological drivers ($d\text{DIC}/dt_{\text{Gas Exchange}}$, $d\text{DIC}/dt_{\text{EP}}$, and
 272 $d\text{DIC}/dt_{\text{Entrainment}}$; $d\text{TA}/dt_{\text{EP}}$, and $d\text{TA}/dt_{\text{Entrainment}}$) and subtract from the weekly overall change
 273 ($d\text{DIC}/dt$; $d\text{TA}/dt$), leaving the biological drivers ($d\text{DIC}/dt_{\text{Biology}}$; $d\text{TA}/dt_{\text{Biology}}$), as the remainder.
 274 The sections below describe how each of the right hand side terms in these equations are
 275 calculated. All right-hand side terms in both budgets are calculated at weekly resolution. We
 276 smooth the observed carbonate system time series used in the budget with a three week running
 277 mean to remove high-frequency variability.

$$278 \quad \frac{d\text{DIC}}{dt} = \frac{d\text{DIC}}{dt} |_{\text{Gas Exchange}} + \frac{d\text{DIC}}{dt} |_{\text{EP}} + \frac{d\text{DIC}}{dt} |_{\text{Entrainment}} + \frac{d\text{DIC}}{dt} |_{\text{Biology}} \quad (1)$$

$$279 \quad \frac{d\text{TA}}{dt} = \frac{d\text{TA}}{dt} |_{\text{EP}} + \frac{d\text{TA}}{dt} |_{\text{Entrainment}} + \frac{d\text{TA}}{dt} |_{\text{Biology}} \quad (2)$$

280 3.2.1 Gas Exchange

281 The rate of DIC change due to gas exchange is calculated from the measured partial pressure of
 282 carbon dioxide ($p\text{CO}_2$) in the atmosphere and surface waters, wind speed, temperature, and
 283 salinity, with positive values indicating a flux from the atmosphere into the ocean (eq. 3).

$$284 \quad \frac{d\text{DIC}}{dt} |_{\text{Gas Exchange}} = k * K_H * (p\text{CO}_{2\text{Air}} - p\text{CO}_{2\text{Seawater}}) * \rho \quad (3)$$

285 The piston velocity (k) is calculated using the Ho et al. (2006) wind speed-dependent gas transfer
286 parameterization, implemented in the MATLAB `gas_toolbox` (Manning and Nicholson, 2022)
287 and the Schmidt constant (Wanninkhof, 1992). Of the OOI moored assets, the surface buoy faced
288 the most challenges with continuous data collection, limiting the ability to use directly-measured
289 meteorological data. Therefore, ERA5 products from the nearest grid cell (60°N, 39.5°W) are
290 used for hourly sea surface temperature and 10m wind speeds (calculated from v - and u -winds at
291 10m, Hersbach et al., 2020). The ERA5 winds match well with the OOI 10m measured wind
292 speeds, when available (Fig. S9).

293 The solubility of CO_2 is calculated using the temperature and salinity dependent constant (K_H)
294 from Weiss (1974). The mixed layer seawater $p\text{CO}_2$ data is calculated as described in section
295 3.1.4. The air $p\text{CO}_2$ data is from NOAA's Global CarbonTracker gridded daily average product
296 at 59°N, 40.5°W using CO_2 mole fraction, humidity, and barometric pressure (CT_2022 and CT-
297 NRT.v2023-4, Jacobson et al., 2023, comparison with Pro-Oceanus air $p\text{CO}_2$, Fig. S10).
298 Multiplying by the density (ρ) leaves us with the amount of carbon exchanged in units of mmol
299 $\text{m}^{-2} \text{d}^{-1}$.

300 3.2.2 Physical Transport

301 The fixed nature of moored sensors necessitates a Eulerian approach in order to account for the
302 influence of horizontal and vertical transport on mixed layer DIC. The primary physical
303 influence is entrainment, whereby the mixed layer increases in depth and adds water from below
304 into the mixed layer. When the mixed layer shoals (detrainment), the mixed layer DIC
305 concentration is not impacted. Given that this study site is in the center of the Irminger Gyre
306 where there are low horizontal velocities, we exclude horizontal transport from our budget (Fig.
307 1). We also exclude estimating the budget contributions of vertical diffusion and vertical
308 velocity. Although these have been shown to be significant in mixed layer mass balance budgets
309 in other regions (such at North Pacific and North Pacific subtropical gyre, Fassbender et al.
310 2016; Knor et al. 2023), measured values for these terms have been shown to be low in the
311 Irminger Sea and exceptionally deep winter convection at this site means that entrainment
312 dominates over these second-order processes (Fratantoni, 2001; Painter et al., 2014; Våge et al.,
313 2008).

314 In order to calculate the rate of physical entrainment, we use weekly mixed layer depths. There
 315 has been extensive discussion within the literature regarding how to define the mixed layer depth
 316 with respect to timescales of mixing and biological processes (Carranza et al., 2018; Carvalho et
 317 al., 2017; Lacour et al., 2019). We use a combination of methods including temperature
 318 thresholds and bio-optical methods to determine the mixed layer depth depending on the time of
 319 year and availability of both OOI and external data (Table S2), a full explanation of which can be
 320 found in the Supplementary Information, Section 6. We determine the effects of entrainment on
 321 mixed layer DIC, TA, and salinity using a one-dimensional model that accounts for the influence
 322 of mixing between the prior mixed layer and newly-entrained waters, calculated at weekly time
 323 steps. This model uses the mixed layer time series to calculate physical entrainment rates and
 324 accounts for the salinity, DIC, and TA of waters being entrained into the mixed layer using DIC
 325 and TA estimated from OOI glider and wire-following profiler oxygen, temperature, and salinity
 326 using the CONTENT model (Bittig et al., 2018). The entrainment model tracks closely with
 327 observed DIC concentrations in the fall, showing that the increase in mixed layer DIC during this
 328 period of time is primarily the result of the entrainment of high DIC waters (Fig. S12).

329 3.2.3 Evaporation and Precipitation

330 To account for dilution and concentration effects on DIC and TA due to evaporation and
 331 precipitation, we find the difference between the observed change in salinity over time and the
 332 entrainment-modeled change in salinity over time (Fassbender et al., 2016; Haskell et al., 2020).

333 We attribute the difference between the observations and the modeled change to evaporation and
 334 precipitation, as any change in salinity not due to entrainment is the result of these surface
 335 processes in our model, again assuming minimal horizontal advection. We multiply the
 336 difference in the two by the ratio of DIC (and TA) to absolute salinity on the first day of each
 337 deployment, working under the assumption that the ratio that salinity changes due to evaporation
 338 and precipitation is the same for DIC and TA (eq. 4). The same process is followed for TA.

$$339 \quad \frac{d(DIC,TA)}{dt} \Big|_{EP} = \left(\frac{dSal}{dt} - \frac{dSal}{dt} \Big|_{Entrainment} \right) * \frac{(DIC,TA)}{Sal} \Big|_{t=1} \quad (4)$$

340 3.2.4 Biological Processes

341 The biological drivers are calculated as the residual terms of equations 1 and 2. These drivers are
 342 net community production (NCP) via photosynthesis and respiration and calcium carbonate
 343 (CaCO₃) formation and dissolution (eq. 5).

$$344 \quad \frac{d(DIC,TA)}{dt} \Big|_{Biology} = \frac{d(DIC,TA)}{dt} \Big|_{NCP} + \frac{d(DIC,TA)}{dt} \Big|_{CaCO_3} \quad (5)$$

345 In order to separate the soft tissue processes (photosynthesis and respiration, which influence
 346 NCP) from calcium carbonate production and dissolution, we leverage the known production
 347 ratio of CO₂ and H⁺ (117 to -17) from respiration using 1 mole of phosphate (HPO₄²⁻) (Anderson
 348 & Sarmiento, 1994; Fassbender et al., 2016). This formation and precipitation of CaCO₃
 349 influences TA and DIC in a 2:1 ratio. This allows us to calculate the influence of NCP on the
 350 mixed layer DIC budget (eq. 6). We also calculate weekly and annual NCP within the
 351 seasonally-varying mixed layer by integrating to the weekly mixed layer depth.

$$352 \quad \frac{dDIC}{dt} |_{NCP} = \frac{\left(\frac{dTA}{dt} |_{Bio} - 2 * \frac{dDIC}{dt} |_{Bio} \right)}{-2 + \frac{-17}{117}} \quad (6)$$

353 3.3 Uncertainty

354 Here we present the calculated uncertainties of the calibrated DIC, TA, and *p*CO₂ time series, as
 355 well as uncertainties of terms in the DIC budget (Table 1). The uncertainties of the measured
 356 parameters propagated through to calculate these values can be found in the Supplementary
 357 Information (Table S3). Temperature and salinity measurement errors are slight but do factor
 358 into all of the calculated parameter uncertainties.

359 The uncertainty of the mooring DIC time series is estimated using the CO2SYS error
 360 propagation, with temperature, salinity, pressure, pH, *p*CO₂, and estimated TA uncertainties as
 361 inputs (Orr et al., 2018). Uncertainty for estimated TA is generated from the LIAR model (Carter
 362 et al., 2018). A limitation of deriving total alkalinity from salinity is that mixed layer TA can
 363 change independent of salinity when biological formation of calcium carbonate occurs. Remote
 364 sensing shows calcification rates exceeding 1 mmol C m⁻² and very high interannual variability
 365 in calcification rates in the Irminger Sea, which could lead to our DIC estimates being slightly
 366 high in late summer (Hopkins et al., 2015). Despite this, the close agreement between the surface
 367 sensor *p*CO₂ and surface *p*CO₂ calculated from DIC and TA suggest that the impact of this
 368 uncertainty in TA is small (Fig. S8).

369 There is uncertainty in each of the terms of the mass balance budget (eq. 1 & 2, Table 1). The
370 95% confidence bounds of entrainment are calculated by taking the minimum and maximum
371 values from the entrainment model runs with a combination of systematically over- and under-
372 estimated mixed layer depths and the lower and upper uncertainties of the DIC concentration
373 below the mixed layer. The evaporation-precipitation uncertainty is estimated using a Monte
374 Carlo simulation iterated 5000 times with the salinity and DIC entrainment uncertainty and the
375 uncertainty of the DIC concentration on the first week of each deployment. The gas exchange
376 uncertainty is also calculated using a Monte Carlo simulation to account for the uncertainties in
377 temperature, salinity, $p\text{CO}_2$ of air and seawater, and a 20% assigned uncertainty in the gas
378 transfer coefficient to account for uncertainty in the wind speed data as well as in the
379 parameterized relationship between wind speed and gas transfer (Ho et al., 2006; Wanninkhof,
380 2014; Yang et al., 2021). Calculating the biological processes as the remainder from the mass
381 balance budget means that the biological term contains the accumulation of the uncertainties
382 from all the other budget terms. We use a wrap-around Monte Carlo containing all the previously
383 discussed uncertainties (Table 1) in which we subtract the physical transport, EP, and gas
384 exchange terms from the overall change in DIC in order to determine the uncertainty in the
385 biological processes.

386

387

388

389

390

391

392

393

394

395

396

397

398

399 Table 1.

400 *Uncertainties of analyzed parameters*

Time series	Uncertainty	Primary sources of error
Calibrated DIC ($\Delta\text{DIC}_{\text{Observed}}$)	11.2-11.6 mmol m^{-3}	Measurement of pH and $p\text{CO}_2$, calibration of DIC time series
TA ($\Delta\text{TA}_{\text{Observed}}$)	9.7-10.2 mmol m^{-3}	Estimate from LIAR model, measurement of salinity
$p\text{CO}_2$	2 μatm	Measurement of surface $p\text{CO}_2$, calculation from DIC and TA
$\Delta\text{DIC}_{\text{Entrainment}}$	8.7-10.3 mmol m^{-3}	DIC concentration below the mixed layer, mixed layer depth
$\Delta\text{DIC}_{\text{EP}}$	1.1-2.0 mmol m^{-3}	entrainment salinity model from MLD and glider/WFP salinity measurements, ratio of DIC/TA to salinity on first day of deployment
$\Delta\text{DIC}_{\text{GE}}$	0.02-0.05 mmol m^{-3}	air and sea $p\text{CO}_2$, wind speed, gas transfer coefficient
$\Delta\text{DIC}_{\text{NCP}}$	14.7-16.0 mmol m^{-3}	Combined uncertainty of all other budget terms, stoichiometry of photosynthesis-respiration and calcium carbonate formation-dissolution
$\Delta\text{DIC}_{\text{CaCO}_3}$	28.5-30.5 mmol m^{-3}	Combined uncertainty of all other budget terms, stoichiometry of photosynthesis-respiration and calcium carbonate formation-dissolution

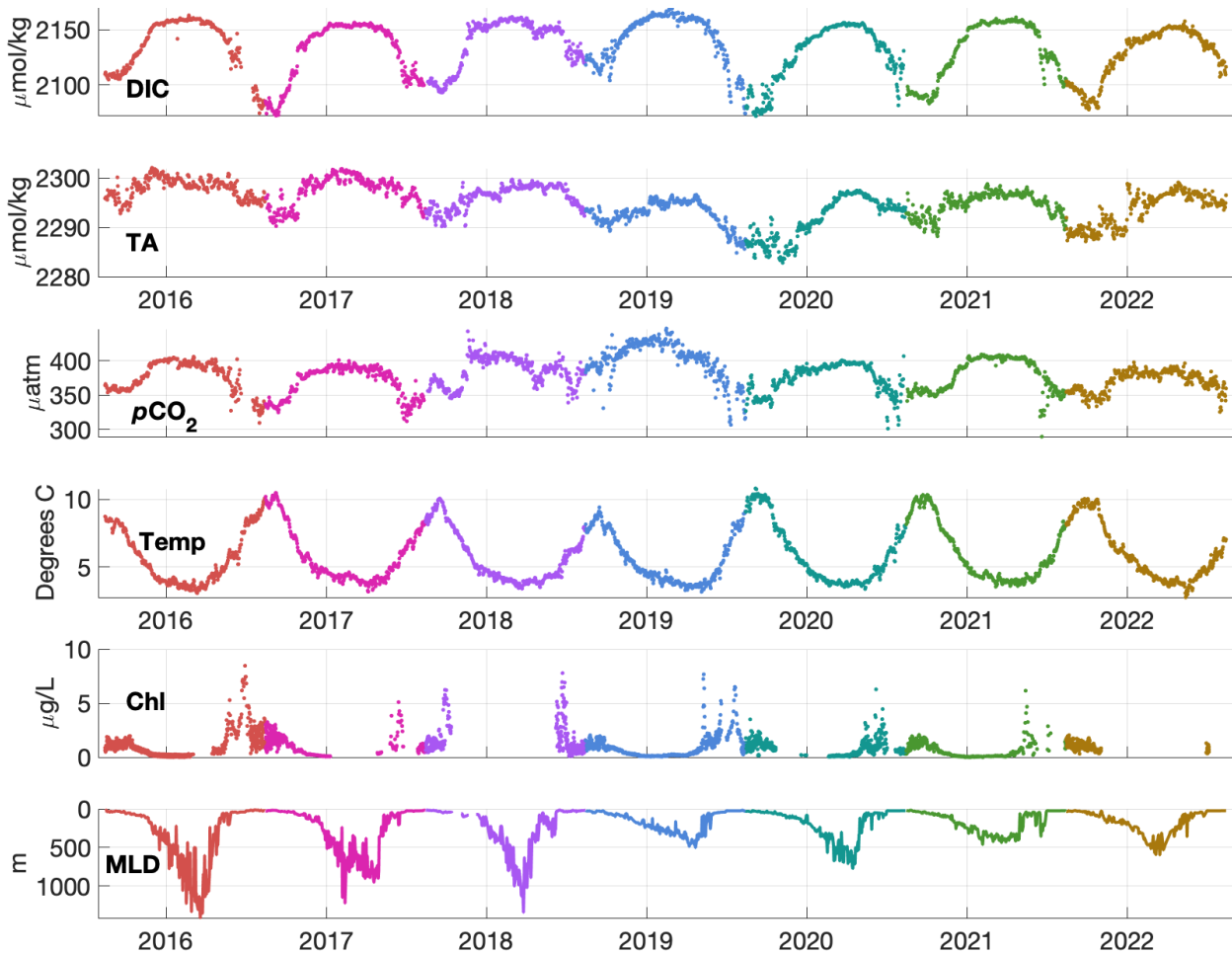
401 *Note.* Values shown are the range of yearly means over all seven years in the time-series.

402 **4 Results and Discussion**

403 4.1 Mixed layer time series

404 Here we present mixed layer carbonate system variables (DIC, TA, and $p\text{CO}_2$) as well as their
 405 potential drivers (mixed layer depth, temperature, and chlorophyll-*a*) in the central Irminger Sea
 406 (Fig. 3). The carbonate system variables follow a similar annual cycle of highs and lows, with
 407 the minimums occurring in late summer at the end of the productive season, then
 408 climbing throughout the fall to a maximum in winter, after which they are drawn down again in
 409 the spring (Fig. 3).

410



411

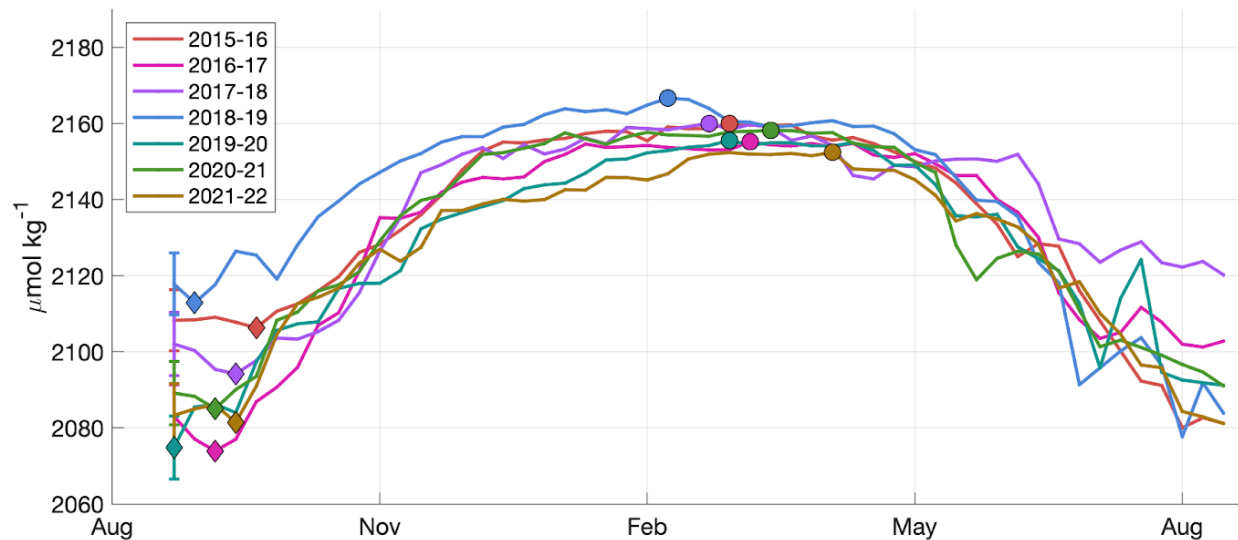
412 **Figure 3.** Daily mixed layer DIC, TA, $p\text{CO}_2$, temperature, chlorophyll-*a*, and mixed layer time
 413 series. Colors correspond with annual cycles beginning on August 15th.

414 In the Irminger Sea, sea surface temperatures vary significantly, from around 3°C in the winter
415 up to 12°C in the summer. The partial pressure of CO₂ ($p\text{CO}_2$) is significantly affected by
416 temperature (Weiss, 1974); if there were no biological processes reducing the $p\text{CO}_2$, we would
417 expect to see the highest $p\text{CO}_2$ in the summer and the lowest $p\text{CO}_2$ in the winter, as solubility
418 declines as temperature increases (Takahashi et al., 2002). Instead, as has been well documented
419 in prior literature, the greatest $p\text{CO}_2$ are recorded in the winter and lowest are found in the
420 summer due to biological drawdown, indicating that biophysical effects, rather than temperature,
421 are the primary drivers of $p\text{CO}_2$ at our site (Bates et al., 2014; Landschützer et al., 2018;
422 Takahashi et al., 2002).

423 The influence of vertical mixing and primary productivity can be clearly seen on the other,
424 temperature-insensitive, carbonate system parameters (DIC and TA). In the spring and summer,
425 the mixed layer is strongly stratified and high chlorophyll concentrations are recorded. At the
426 same time, DIC concentrations reach their minimum in the annual cycle, ranging from 2074±8 to
427 2110±8 $\mu\text{mol kg}^{-1}$ during our period of observation (Fig. 4). It is important to note that while
428 chlorophyll concentration does indicate primary productivity, the amount of inorganic carbon
429 being utilized is not directly reflected, as widely varying chlorophyll to carbon ratios occur at
430 different global locations, depths in the water column, and times of year (Sathyendranath et al.,
431 2009). Due to infrastructure failures, the sensors are not always successful in capturing the entire
432 spring bloom; however, in situ chlorophyll measured by fluorometry and satellite chlorophyll
433 data confirm annual spring and fall blooms at the Irminger site (Painter et al., 2014).

434 In the fall, convection begins and the mixed layer starts deepening. The Irminger Sea's uniquely
435 deep mixed layers are not observed until later in the season, with mixed layer depths rarely
436 exceeding 100m before mid November. Most of the interannual variability in mixed layer depth
437 occurs in the winter, both in the timing of deepening and the maximum depth reached. Some
438 years, such as 2015-2016, experience early and rapid deepening, but the deepest sustained winter
439 mixing is usually reached in mid to late March, ranging from ~400 to ~1300m. The patterns
440 observed here match previous analysis of MLDs in this region (de Jong et al. 2024). Shoaling in
441 the spring begins gradually and then intensifies, going from near maximum depths to less than
442 100m over the span of a few weeks from early April to mid-May (Sterl and de Jong, 2022).
443 During this time, we observe repeated shoaling and deepening, a process previously observed in
444 the North Atlantic (Lacour et al., 2019). After the final shoaling, increased chlorophyll
445 concentrations are observed again. It should be noted that the seven year OOI time series
446 captures a period of time in which there is particularly strong winter convection (3 winters
447 deeper than 1000m), even for the Irminger region. Before the OOI time series, winter mixed
448 layer depths for only one year between 2002 and 2013 (2011-2012) were close to 1000m (de
449 Jong et al., 2024).

450 The mixed layer DIC signal generally increases and decreases in concert with the seasonal
 451 changes in mixed layer depth. The increase in mixed layer DIC coincides with mixed layer
 452 deepening (Fig. 3). It is rapid in mid-September through mid-November and then continues to
 453 rise with a less significant slope between mid-February to late March, when it reaches the
 454 maximum annual concentration. The DIC concentration begins to decrease moderately in the late
 455 winter and then decreases more rapidly in late April to mid-May, coinciding with high
 456 chlorophyll concentrations.



457

458 **Figure 4.** The annual seasonal cycle of DIC concentration in the mixed layer, beginning on
 459 August 15th. The diamonds are the lowest DIC concentration at the end of the productive season
 460 and the circles are the annual DIC maximum. The error bars at the beginning of the time series
 461 show uncertainty derived from the Monte Carlo simulation and apply across the time
 462 series. Gaps less than 2 weeks have been filled via linear interpolation.

463 The amount of fall-winter increase and spring-summer decrease of mixed layer DIC varies from
 464 year to year. While there is a broad interannual range in the amplitude of the DIC seasonal cycle
 465 (mean 68 ± 11 , range 54-81 $\mu\text{mol kg}^{-1}$), the range of the winter maximum weekly DIC
 466 concentration is only 14 $\mu\text{mol kg}^{-1}$ (Fig. 4). This is almost within the uncertainty of the mixed
 467 layer DIC time series ($\sim 11 \mu\text{mol kg}^{-1}$), making the annual maximum DIC effectively
 468 indistinguishable from year to year. The summer minimum is far more variable, reflecting more
 469 variability in the impact of biological DIC drawdown than winter convection on the mixed layer
 470 DIC annual cycle. The DIC seasonal cycle amplitude is similar to previous measurements in the
 471 Irminger Sea ($\sim 60 \mu\text{mol kg}^{-1}$, Bates et al., 2014) and other high latitude regions including the
 472 North Pacific ($\sim 56 \pm 7 \mu\text{mol kg}^{-1}$ at Ocean Station Papa, $73 \pm 2 \mu\text{mol kg}^{-1}$ in the Kuroshio
 473 Extension, Fassbender et al., 2016, 2017) and Western Antarctic Peninsula ($\sim 55 \mu\text{mol kg}^{-1}$, Yang
 474 et al., 2021), however the interannual variability observed in the Irminger Sea is higher.

475

476 4.2 Mixed Layer Carbon Mass Balance

477 To investigate the specific drivers of the annual carbonate system chemistry cycle and its
478 interannual variability, we use a mass balance approach. Comparison among each of the terms
479 influencing the DIC seasonal cycle (eq. 1) shows that entrainment of deep waters and biological
480 processes have the greatest impact on the DIC seasonal cycle, with gas exchange and
481 evaporation-precipitation playing relatively minor roles (Fig. 5).

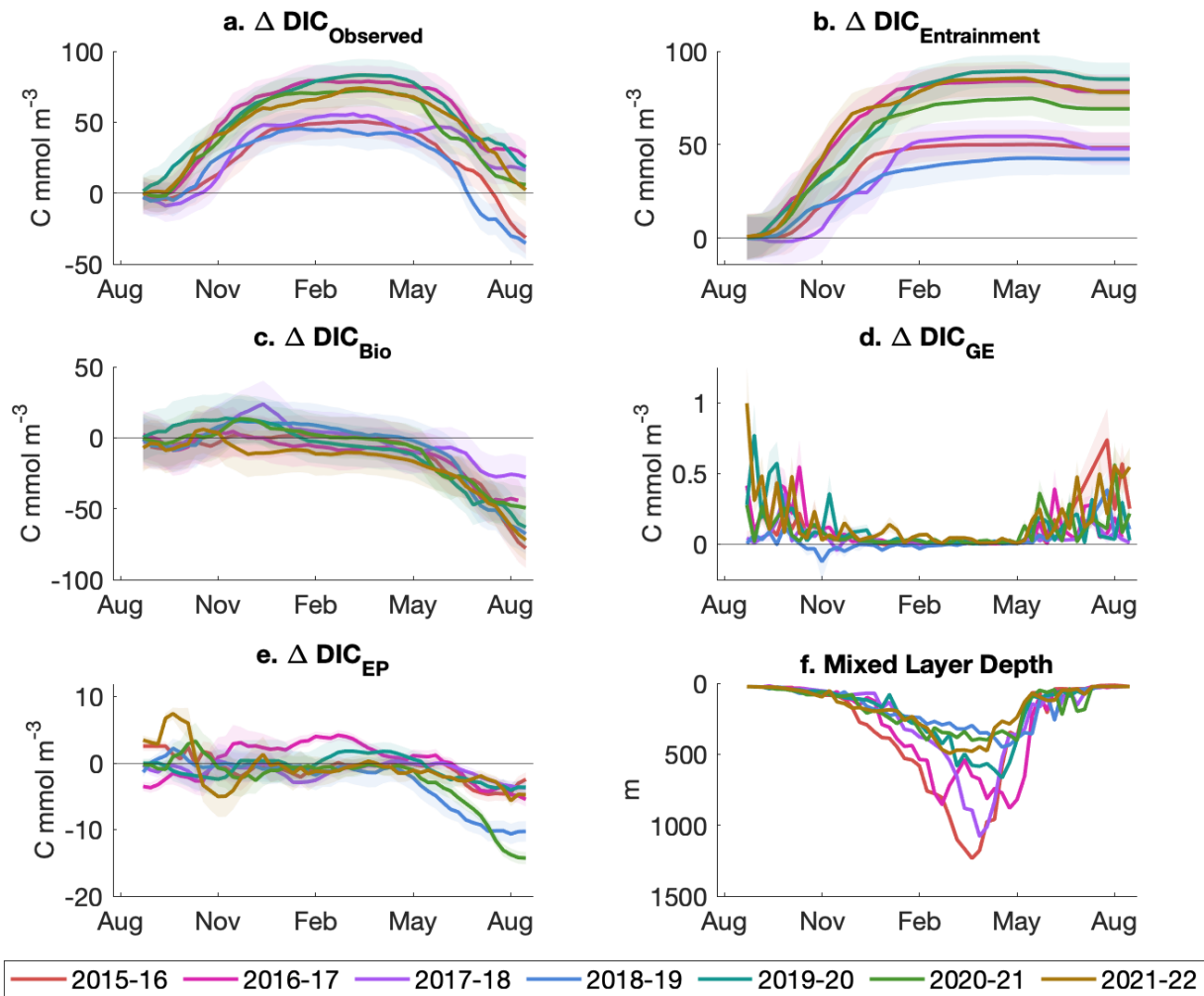
482

483

484

485

486



488 **Figure 5.** Influences of each term in the mixed layer DIC mass balance budget (eq. 1) on a) the
 489 observed change in DIC concentration since Aug. 15 over each of the seven years in the time
 490 series. Changes in mixed layer DIC are driven by: b) the change in DIC concentration due to
 491 entrainment, c) the change in DIC concentration due to biological processes, d) the change in
 492 DIC concentration due to gas exchange, and e) the change in DIC concentration due to
 493 evaporation and precipitation, each presented as the cumulative change since August 15 in each
 494 year of the time series. Each of these terms is calculated within the seasonally-varying mixed
 495 layer depth at weekly resolution (f). Note that the y-axes are scaled differently on each plot.

496 While gas exchange has very little impact on the overall mixed layer DIC concentration, the
497 average total addition of DIC to the mixed layer due to CO₂ influx from the atmosphere is 2.1
498 mol ± 1.1 mol m⁻² yr⁻¹ over our seven year period. A recent *p*CO₂ climatological product reports
499 a mean of 3.0±0.7 mol m⁻² yr⁻¹ during our study period (range 2.1-3.8 mol m⁻² yr⁻¹, Landschützer
500 et al. 2020). This matches our observations within the uncertainty, and the somewhat higher
501 values can likely be attributed to our differing choice of gas transfer parameterization
502 (Atamanchuk et al., 2020). From our observational data, the years with the lowest annual carbon
503 uptake via gas exchange are also the years when the maximum mixed layer depth exceeds
504 1000m (2015-2016 and 2017-2018), potentially indicating that the continued entrainment of high
505 DIC waters suppresses winter uptake driven by cooling waters. Gas exchange occurs at the
506 surface and therefore has the highest potential to impact DIC concentration when the mixed layer
507 is shallowest (has the least volume). The most significant stratification occurs during the summer
508 when the difference between air and seawater *p*CO₂ is greatest. These conditions would support
509 strong influx; however the winds tend to be slow this time of year and do not drive vigorous gas
510 exchange. In the winter when extremely high winds occur, the volume of the mixed layer has
511 expanded by almost two orders of magnitude, so even the fastest gas exchange has very little
512 impact on overall mixed layer DIC concentration, making gas exchange (dDIC/dt_{GE}) the least
513 impactful driver of changes in mixed layer DIC (Fig. 5d).

514 The impact of evaporation and precipitation on DIC concentration ($dDIC/dt_{EP}$) is also low
515 throughout the year, and, as with gas exchange, has the greatest impact when the water column is
516 stratified due to its influence occurring only at the air-sea interface. The impact of evaporation
517 and precipitation varies from year to year but, on average, mild dilution occurs in the summer
518 months, reducing DIC concentration by $6.4 \pm 4.3 \text{ mmol m}^{-3} \text{ yr}^{-1}$ (Fig. 5e). The dominant driver of
519 DIC increase in the mixed layer is entrainment ($dDIC/dt_{Entrainment}$), which increases mixed layer
520 DIC by $64 \pm 17 \text{ mmol m}^{-3} \text{ yr}^{-1}$. The DIC concentration rises concurrently with an increase in
521 mixed layer depth as high DIC waters from below mix with the DIC-depleted surface waters.
522 The concentration rises rapidly even though the mixed layer does not deepen extremely quickly
523 because of the outsized role of the addition of water into the shallow end-of-summer mixed layer
524 and the very low summer DIC concentration. A mixed layer of 20m with DIC of 2080 mmol m^{-3}
525 that entrains 80m of 2170 mmol m^{-3} DIC waters then has a DIC concentration of 2152 mmol m^{-3} ,
526 an increase of 72 mmol m^{-3} and roughly the amplitude of the seasonal cycle. Alternatively, a
527 100m mixed layer with DIC of 2152 mmol m^{-3} that entrains 200m of 2170 mmol m^{-3} DIC waters
528 results in a DIC concentration of 2164 mmol m^{-3} , only increasing the overall concentration by 8
529 mmol m^{-3} . The total amount of carbon added via entrainment varies based on each year's
530 maximum mixed layer depth, but brings the surface concentration close to the same value each
531 winter ($\sim 2220 \text{ mmol m}^{-3}$). While we have primarily considered the extremely deep winter
532 convection for its role in returning carbon to the surface ocean in the winter, the subsequent
533 springtime shoaling of the mixed layer detrains water that contains both inorganic and organic
534 carbon in a process known as the seasonal mixed layer pump (Dall'Olmo et al., 2016). The
535 intraseasonal and seasonal mixed layer pump has been shown to significantly contribute to
536 carbon export in the subpolar North Atlantic, a process which is likely occurring at our study site
537 (Lacour et al., 2019).

538 Biological processes ($dDIC/dt_{Biology}$) lead to a net drawdown of DIC on an annual basis (Fig. 5c),
539 with photosynthesis and calcium carbonate formation outpacing respiration and calcium
540 carbonate dissolution. In the fall, the influence of biology is near zero, with slight heterotrophy in
541 some years and autotrophy in others; however, the uncertainty crosses zero most years,
542 obscuring any definitive fall trend. Each winter shows the same pattern: from February to May
543 there is a slow but persistent decrease in DIC concentration due to biological processes. Once the
544 mixed layer shoals, there is much more rapid drawdown, which comprises the bulk of the change
545 in concentration due to biology over the annual cycle. While we cannot quantitatively relate the
546 measured chlorophyll to DIC drawdown, the chlorophyll data clearly supports the rapid
547 reduction due to primary productivity in the late spring (Fig. 3).

548

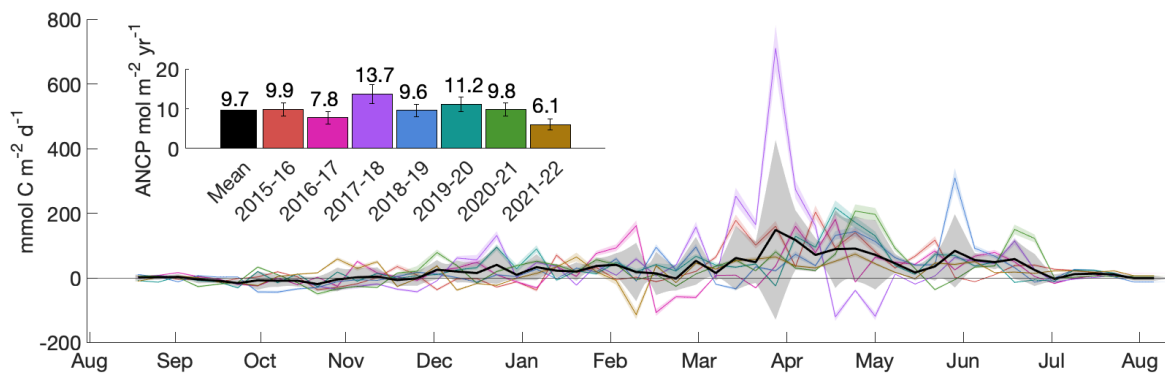
549

550

551 4.3 Annual Net Community Production

552 The annual net community production (ANCP) within the mixed layer is the upper bound on the
 553 amount of carbon removed from the surface ocean by the biological pump each year ($NCP = -$
 554 ΔDIC_{NCP}). The choice of depth of integration for calculating ANCP varies depending on the
 555 method of export research. This can lead to discrepancies when intercomparing ANCP rates,
 556 particularly in high latitude regions with deep winter convection, where a significant fraction of
 557 the carbon removed from the mixed layer during spring and summer is subsequently respired
 558 within the seasonal thermocline and re-entrained into the mixed layer during winter (Palevsky &
 559 Doney, 2018). Here, we leverage our mixed layer DIC budget to determine the seasonal cycle
 560 and interannual variability of NCP and ANCP integrated to the seasonally varying mixed layer
 561 depth. While not all of this NCP will lead to long-term carbon sequestration at depth, this value
 562 is of particular interest as the surface ocean pCO_2 , and in turn the influx of carbon from the
 563 atmosphere to the upper ocean, is strongly influenced by NCP-driven changes in mixed layer
 564 DIC concentration.

565 We find net autotrophy in the Irminger Sea for most of the year, with the highest NCP rates
 566 occurring in the early spring prior to mixed layer shoaling (Fig. 6). NCP rates in this paragraph
 567 are the mean and standard deviation across all 7 years. In the late summer into the late fall, we
 568 observe NCP from near neutral to mildly heterotrophic ($-5 \pm 17 \text{ mmol m}^{-2} \text{ d}^{-1}$ from Aug. 15 to
 569 Nov. 15). In January, there is a transition to autotrophy with an NCP of $24 \pm 43 \text{ mmol m}^{-2} \text{ d}^{-1}$ until
 570 the end of February. By April, shoaling has begun and the mixed layer is strongly autotrophic,
 571 with an NCP of $77 \pm 26 \text{ mmol m}^{-2} \text{ d}^{-1}$ from the beginning of April to mid-May. From then until
 572 August 15th, the mixed layer is relatively shallow and continues to be autotrophic at a much
 573 lower NCP of $28 \pm 24 \text{ mmol m}^{-2} \text{ d}^{-1}$.



574

575 **Figure 6.** Net community production (NCP) rates integrated to the seasonally-varying mixed
 576 layer depth. The colored lines show each individual year, the thick black line shows the mean
 577 across all years, and the gray shading is one standard deviation of the interannual mean. The bar
 578 chart shows total annual net community production (ANCP). ANCP error bars are the
 579 uncertainty as calculated through Monte Carlo analysis (details in Section 3.3).

580 We find that the central Irminger Sea has high ANCP as well as high interannual variability, with
581 an annual mean of $9.7 \pm 1.7 \text{ mol C m}^{-2} \text{ yr}^{-1}$ (\pm signifies propagated error, not standard deviation,
582 Fig. 6). The highest ANCP recorded during our study period was $13.7 \pm 2.3 \text{ mol C m}^{-2} \text{ yr}^{-1}$ during
583 2017-2018. This year had a later-than-average onset of mixed layer deepening, resulting in a
584 shallow fall mixed layer that caused the high fall chlorophyll concentration without a high depth-
585 integrated rate of NCP. This is the only year with a decrease in DIC due to entrainment, likely
586 indicating photosynthesis below the mixed layer during the large fall bloom. There is a late fall
587 respiration signal, potentially fueled by sinking organic carbon from the fall bloom. 2017-2018
588 had very deep winter convection, as well as a decrease in DIC due to NCP from early March to
589 mid-April that outpaced the time series mean (12 mmol m^{-3} reduction in DIC over this time
590 period compared to the time series mean of 5 mmol m^{-3}), which together resulted in high
591 integrated NCP over this time period and for the yearly total. The lowest ANCP recorded
592 occurred during 2021-2022 ($6.0 \pm 1.3 \text{ mol m}^{-2} \text{ yr}^{-1}$), which also had the earliest spring shoaling of
593 the observed period (Fig. 3). DIC increased in the late fall due to both entrainment and
594 respiration and there were relatively low NCP rates in the winter and early spring. These findings
595 indicate that the depth and timing of winter mixing substantially impacts the overall annual net
596 community production; however the rate of DIC drawdown by biology prior to mixed layer
597 shoaling is also an important control on ANCP.

598 This study adds to a growing body of research using DIC and TA as mass balance tracers to
599 quantify ANCP within the seasonally varying mixed layer depth. The majority of sites have
600 yielded lower ANCP than we find in the Irminger Sea ($2 \pm 1 \text{ mol C m}^{-2} \text{ yr}^{-1}$ at in the North
601 Pacific, $1.2 \pm 2.8 \text{ mol C m}^{-2} \text{ yr}^{-1}$ in the North Pacific subtropical gyre, and $2.8 \pm 2.4 \text{ mol C m}^{-2} \text{ yr}^{-1}$
602 on the West Antarctic Peninsula shelf; Fassbender et al., 2016; Knor et al., 2023; Yang et al.,
603 2021). However, in the Kuroshio extension in the North Pacific, ANCP was $7 \pm 3 \text{ mol C m}^{-2} \text{ yr}^{-1}$
604 (Fassbender et al., 2017). The Kuroshio site has the deepest winter mixed layer depths of other
605 sites where these methods have been used (up to 300m), and similarly to the Irminger Sea, there
606 are extremely high NCP rates seen in early spring as a result. A mixed layer carbon budget in the
607 eastern subpolar North Atlantic (Porcupine Abyssal Plain site, 49°N , 16.5°W) found NCP within
608 the seasonally-varying mixed layer of $6.4 \pm 1.1 \text{ mol m}^{-2} \text{ yr}^{-1}$, with over two thirds of the
609 production occurring prior to the spring shoaling of the mixed layer, a similar seasonal
610 partitioning and annual magnitude as at our site (Kortzinger et al., 2008). Kortzinger et al. also
611 found that 40% of the carbon exported from the seasonally-varying mixed layer was
612 subsequently offset by entrainment of respired carbon during deep winter mixing. Reduced
613 ANCP when integrating to the winter mixed layer depth as compared to ANCP within the
614 seasonally-varying mixed layer has been corroborated by oxygen budgets using data from across
615 the subpolar North Atlantic (Quay et al., 2012, 2020). Given the uniquely deep winter mixing in
616 the Irminger Sea, it will be important for future work to contextualize our ANCP results by
617 determining what fraction of this NCP contributes to long-term carbon sequestration, as well as
618 the mechanistic relationship between NCP-driven DIC-drawdown in the mixed layer and air-sea
619 CO_2 flux.

620 Our chemical tracer approach cannot provide insight into the complex ecosystem level dynamics
621 that likely contribute to the observed high interannual variability in ANCP, however there is a
622 clear connection between strong convection and high ANCP. Prior work investigating
623 interannual variability of phytoplankton productivity in the Irminger Sea based on satellite
624 chlorophyll data (which therefore does not capture early spring NCP discussed here) found that
625 the onset of elevated chlorophyll concentrations varies by as much as 30 days (Henson et al.,
626 2006). Their analysis found that timing of spring mixed layer shoaling influenced the timing and
627 magnitude of the spring bloom; stormier winters with a high number of days with gale-force
628 winds in turn delayed spring stratification, corresponding to later onset of elevated chlorophyll
629 and lower peak chlorophyll concentrations (Henson et al., 2006). However, our work shows
630 significant DIC drawdown by NCP within the deep late winter-early spring mixed layer, prior to
631 mixed layer shoaling and increase in surface chlorophyll concentrations. Our finding of elevated
632 NCP during deep winter mixing is consistent with the disturbance-recovery spring bloom
633 hypothesis, in which the decoupling of zooplankton predator and prey during deep mixing
634 enables enhanced primary productivity due to relief of grazing pressure (Behrenfeld & Boss,
635 2014). Historically, increased light availability with a shoaling mixed layer has been thought to
636 be the catalyst of increased phytoplankton growth (Sverdrup 1953), however more recent work
637 has demonstrated that though high chlorophyll concentrations may be driven by this critical
638 depth hypothesis, a combination of more complex ecosystem interactions caused by winter
639 mixing are at play (Behrenfeld & Boss, 2014 and references within; Mignot et al., 2018). Our
640 results suggest that deeper mixed layers in the later winter and early spring may actually drive
641 higher ANCP, potentially the result of inhibition of grazing due to mixing.

642

643

644

645

646

647

648

649

650

651

652 **5. Conclusions**

653 This work constructs the first long term time series of the inorganic carbon system in the
654 subpolar North Atlantic using daily measurements of the carbonate system. Strong biological
655 drawdown is the primary removal mechanism of inorganic carbon from the mixed layer.
656 Increases in mixed layer DIC are primarily controlled by entrainment of high DIC waters as the
657 mixed layer deepens due to winter convection. Similar maximum DIC concentrations are found
658 each winter despite interannual variability in winter mixing, implying that variations in the depth
659 of winter convection do not drive wintertime mixed layer DIC concentrations. While previous
660 analysis at this site has emphasized the role of deep winter mixing reintroducing respired carbon
661 to the mixed layer that has been previously exported (Palevsky and Nicholson, 2018), we find
662 that strong NCP in the late winter and early spring begins reducing DIC concentration prior to
663 shoaling in all years, such that years with extremely deep convection actually drive higher ANCP
664 from the seasonally-varying mixed layer than those with shallower convection. The highest rates
665 of NCP occur prior to the appearance of high chlorophyll concentrations, highlighting the utility
666 of in situ sensing of carbonate parameters rather than relying on chlorophyll measurements as a
667 proxy for biological productivity in the mixed layer. It is probable that the detrainment of water
668 containing freshly produced organic carbon in the spring contributes to a high magnitude of
669 carbon export, a subject which warrants further exploration.

670 The average annual net community production within the seasonally-varying mixed layer is
671 $9.7 \pm 1.7 \text{ mol C m}^{-2} \text{ yr}^{-1}$ and ranges from 6.0 to $13.7 \text{ mol C m}^{-2} \text{ yr}^{-1}$ over the 7-year study period.
672 Sparsity of data often leads to averaging across multiple years in ocean biogeochemistry and
673 specifically when determining ANCP, however doing so can blur the important differences from
674 year to year in both the drivers and magnitude. Averaging across multiple years does not
675 sufficiently capture the complex carbonate system dynamics in the central Irminger Sea, driven
676 by high interannual variability of winter convection and primary productivity. Collecting
677 observational data is both costly and challenging, however if only one year of data is collected or
678 multiple years are averaged together, ANCP in areas with high interannual variability like the
679 Irminger Sea will be misrepresented. This is highly relevant in the context of efforts to detect the
680 emerging impacts of ongoing anthropogenic climate change on biogeochemical cycles relative to
681 baseline natural variability (Henson et al. 2016). The intended 25-year time series of the OOI
682 Irminger Array will provide more information about the interconnected physical and
683 biogeochemical controls on interannual variability in ANCP, as well as potential long-term
684 trends.

685

686

687

688 Acknowledgments

689 The Ocean Observatories Initiative (OOI) is a major facility fully funded by the National Science
690 Foundation (NSF) under Cooperative Agreement No. 1743430, and the Woods Hole
691 Oceanographic Institution OOI Program Office. We thank the many members of the OOI team,
692 as well as the research vessels and crews for annual OOI Irminger Sea turn-around cruises, who
693 have collected and disseminated this time-series dataset. Our work with these data, and
694 collection and analysis of ancillary measurements during OOI turn-around cruises, was
695 supported by the NSF under awards OCE-194607, OCE-1947970, and OCE-2338450.

696 Open Research*697 Data Availability*

698 Ocean Observatories Initiative mooring and glider data used in this analysis are all from the
699 THREDDS Gold Copy catalog
700 (<https://thredds.dataexplorer.oceanobservatories.org/thredds/catalog.html>).
701 Reference designators for each depth and deployment can be found in the OOI Data Explorer
702 (<https://oceanobservatories.org/knowledgebase/how-to-decipher-a-reference-designator/>,
703 <https://dataexplorer.oceanobservatories.org/>). OOI DIC and TA bottle samples were accessed
704 through the OOI Alfresco portal
705 (<https://alfresco.oceanobservatories.org/alfresco/faces/jsp/browse/browse.jsp>).
706

707 DIC and TA bottle samples run at Boston College can be accessed on the Biological and
708 Chemical Oceanography Data Management Office Database (BCO-DMO, [https://www.bco-](https://www.bco-dmo.org/dataset/904722)
709 [dmo.org/dataset/904722](https://www.bco-dmo.org/dataset/904722)). ERA5 Reanalysis hourly sea surface temperature and 10m wind speed
710 data, used for mixed layer calculations and air-sea gas exchange, are from
711 <https://doi.org/10.24381/cds.adbb2d47>. Sea surface height and current data used in Figure 1 are
712 from E.U. Copernicus Marine Service Information, <https://doi.org/10.48670/moi-00148>.
713 NOAA's CarbonTracker data, used in air-sea gas calculations, are from
714 <https://doi.org/10.15138/ffxv-2z26>. Nutrient mean values at our site are from GLODAPv2_2021,
715 accessible at <https://www.ncei.noaa.gov/data/oceans/ncei/ocads/data/0237935/>.
716

717 Software Availability

718 All analyses were conducted in MATLAB from MathWorks. Basic physical oceanographic
719 conversions were done using the Gibbs SeaWater (GSW) Oceanographic Toolbox of TEOS-10,
720 available at <http://www.TEOS-10.org>. Calculations within the carbonate chemistry system used
721 CO2SYS.v2.1, available at <https://zenodo.org/records/3952803#.X0kReGdKhTa>. Predicted DIC
722 and TA were determined using the CONTENT model, accessible at
723 <https://github.com/HCBScienceProducts/CANYON-B>. Gas transfer parameterizations were
724 calculated using the Gas_Toolbox, accessible at <https://zenodo.org/records/545858>.
725
726

727 **References**

- 728 Álvarez, M., Fajar, N. M., Carter, B. R., Guallart, E. F., Pérez, F. F., Woosley, R. J., & Murata,
729 A. (2020). Global Ocean Spectrophotometric pH Assessment: Consistent Inconsistencies.
730 *Environmental Science and Technology*, 54(18), 10977–10988.
731 <https://doi.org/10.1021/acs.est.9b06932>
- 732 Anderson, L. A., & Sarmiento, J. L. (1994). Redfield ratios of remineralization determined by
733 nutrient data analysis. *Global Biogeochemical Cycles*, 8(1), 65–80.
734 <https://doi.org/10.1029/93GB03318>
- 735 Atamanchuk, D., Koelling, J., Send, U., & Wallace, D. W. R. (2020). Rapid transfer of oxygen to
736 the deep ocean mediated by bubbles. *Nature Geoscience*, 13(3), 232–237.
737 <https://doi.org/10.1038/s41561-020-0532-2>
- 738 Bates, N. R., Astor, Y. M., Church, M. J., Currie, K., Dore, J. E., González-Dávila, M.,
739 Lorenzoni, L., Muller-Karger, F., Olafsson, J., & Santana-Casiano, J. M. (2014). A Time-
740 Series View of Changing Surface Ocean Chemistry Due to Ocean Uptake of Anthropogenic
741 CO₂ and Ocean Acidification. *Oceanography*, 27(1), 126–141.
742 <https://doi.org/10.5670/oceanog.2014.16>
- 743 Behrenfeld, M. J., & Boss, E. S. (2014). Resurrecting the ecological underpinnings of ocean
744 plankton blooms. *Annual Review of Marine Science*, 6, 167–194.
745 <https://doi.org/10.1146/annurev-marine-052913-021325>
- 746 Bittig, H. C., Steinhoff, T., Claustre, H., Fiedler, B., Williams, N. L., Sauzède, R., Körtzinger,
747 A., & Gattuso, J. P. (2018). An Alternative to Static Climatologies: Robust Estimation of
748 Open Ocean CO₂ Variables and Nutrient Concentrations from T, S, and O₂ data using
749 Bayesian Neural Networks. *Frontiers in Marine Science*, 5(328), 1–29.
750 <https://doi.org/10.3389/fmars.2018.00328>
- 751 Boss, E., & Behrenfeld, M. (2010). In situ evaluation of the initiation of the North Atlantic
752 phytoplankton bloom. *Geophysical Research Letters*, 37(18).
753 <https://doi.org/10.1029/2010GL044174>
- 754 Boyd, P. W. (2015). Toward quantifying the response of the oceans' biological pump to climate
755 change. *Frontiers in Marine Science*, 2(OCT), 1–15.
756 <https://doi.org/10.3389/fmars.2015.00077>
- 757 Boyd, P. W., Claustre, H., Levy, M., Siegel, D. A., & Weber, T. (2019). Multi-faceted particle
758 pumps drive carbon sequestration in the ocean. *Nature*, 568(7752), 327–335.
759 <https://doi.org/10.1038/s41586-019-1098-2>
- 760 Caldera, K., Akai, M., Brewer, P., Chen, B., Haugan, P., Iwama, T., Johnston, P., Kheshgi, H.,
761 Li, Q., Ohsumi, T., Pörtner, H., Sabine, C., Shirayama, Y., Thomson, J., Barry, J., & Hansen,
762 L. (2018). IPCC Special Report on Carbon Dioxide Capture and Storage. In *IPCC Special*
763 *Report on Carbon Dioxide Capture and Storage*. [https://doi.org/10.1016/b978-1-85617-636-](https://doi.org/10.1016/b978-1-85617-636-1.00012-2)
764 [1.00012-2](https://doi.org/10.1016/b978-1-85617-636-1.00012-2)
- 765 Carranza, M. M., Gille, S. T., Franks, P. J. S., Johnson, K. S., Pinkel, R., & Girton, J. B. (2018).
766 When Mixed Layers Are Not Mixed. Storm-Driven Mixing and Bio-optical Vertical
767 Gradients in Mixed Layers of the Southern Ocean. *Journal of Geophysical Research:*
768 *Oceans*, 123(10), 7264–7289. <https://doi.org/10.1029/2018JC014416>
- 769 Carter, B. R., Feely, R. A., Williams, N. L., Dickson, A. G., Fong, M. B., & Takeshita, Y.
770 (2018). Updated methods for global locally interpolated estimation of alkalinity, pH, and

- 771 nitrate. *Limnology and Oceanography: Methods*, 16(2), 119–131.
772 <https://doi.org/10.1002/lom3.10232>
- 773 Carvalho, F., Kohut, J., Oliver, M. J., & Schofield, O. (2017). Defining the ecologically relevant
774 mixed-layer depth for Antarctica's coastal seas. *Geophysical Research Letters*, 44(1), 338–
775 345. <https://doi.org/10.1002/2016GL071205>
- 776 Cowles, T., Delaney, J., Orcutt, J., & Weller, R. (2010). The Ocean Observatories Initiative:
777 Sustained Ocean Observing Across a Range of Spatial Scales. *Marine Technology Society*
778 *Journal*, 44(6), 54–64.
- 779 Dall'Olmo, G., Dingle, J., Polimene, L., Brewin, R. J. W., & Claustre, H. (2016). Substantial
780 energy input to the mesopelagic ecosystem from the seasonal mixed-layer pump. *Nature*
781 *Geoscience*, 9(11), 820–823. <https://doi.org/10.1038/ngeo2818>
- 782 de Jong, F. M., Oltmanns, M., Karstensen, J., & de Steur, L. (2018). Deep Convection in the
783 Irminger Sea Observed with a Dense Mooring Array. *Oceanography*, 31(1), 50–59.
784 <https://doi.org/10.2307/26307787>
- 785 de Jong, M. F., & de Steur, L. (2016). Strong winter cooling over the Irminger Sea in winter
786 2014–2015, exceptional deep convection, and the emergence of anomalously low SST.
787 *Geophysical Research Letters*, 43(13), 7106–7113. <https://doi.org/10.1002/2016GL069596>
- 788 de Jong, M. F., Fogaren, K. E., Le Bras, I., McRaven, L., & Palevsky, H. I. (2024, in review at
789 JGR:Oceans). Convection in the central Irminger Sea: insights into variability and the roles
790 of surface forcing and stratification from 19 years of high resolution mooring data. *Journal of*
791 *Geophysical Research: Oceans*.
- 792 DeGrandpre, M. D., Wanninkhof, R., McGillis, W. R., & Strutton, P. G. (2004). A Lagrangian
793 study of surface $p\text{CO}_2$ dynamics in the eastern equatorial Pacific Ocean. *Journal of*
794 *Geophysical Research: Oceans*, 109(8). <https://doi.org/10.1029/2003JC002089>
- 795 DeVries, T. (2022). The Ocean Carbon Cycle. *Annual Review of Environment and Resources*,
796 47, 317–341. <https://doi.org/10.1146/annurev-environ-120920>
- 797 Dickson, A. G. (1990). Thermodynamics of the dissociation of boric acid in synthetic seawater
798 from 273.15 to 318.15 K. *Deep-Sea Research*, 37(5), 755–766.
- 799 Emerson, S. (2014). Annual net community production and the biological carbon flux in the
800 ocean. *Global Biogeochemical Cycles*, 28, 1–12. <https://doi.org/10.1002/2013GB004680>
- 801 Fassbender, A. J., Sabine, C. L., & Cronin, M. F. (2016). Net community production and
802 calcification from 7 years of NOAA Station Papa Mooring measurements. *Global*
803 *Biogeochemical Cycles*, 30, 250–267. <https://doi.org/10.1002/2015GB005205>.Received
- 804 Fassbender, A. J., Sabine, C. L., Cronin, M. F., & Sutton, A. J. (2017). Mixed-layer carbon
805 cycling at the Kuroshio Extension Observatory. *Global Biogeochemical Cycles*, 31(2), 272–
806 288. <https://doi.org/10.1002/2016GB005547>
- 807 Fratantoni, D. M. (2001). North Atlantic surface circulation during the 1990's observed with
808 satellite-tracked drifters. *Journal of Geophysical Research: Oceans*, 106(C10), 22067–
809 22093. <https://doi.org/10.1029/2000jc000730>
- 810 Friedlingstein, P., O'Sullivan, M., Jones, M. W., Andrew, R. M., Gregor, L., Hauck, J., Le
811 Quéré, C., Luijkx, I. T., Olsen, A., Peters, G. P., Peters, W., Pongratz, J., Schwingshackl, C.,
812 Sitch, S., Canadell, J. G., Ciais, P., Jackson, R. B., Alin, S. R., Alkama, R., ... Zheng, B.
813 (2022). Global Carbon Budget 2022. *Earth System Science Data*, 14(11), 4811–4900.
814 <https://doi.org/10.5194/essd-14-4811-2022>
- 815 Fogaren, K. E., Palevsky, H. I. (2023) Bottle-calibrated dissolved oxygen profiles from yearly
816 turn-around cruises for the Ocean Observations Initiative (OOI) Irminger Sea Array 2014 –

- 817 2022. Biological and Chemical Oceanography Data Management Office (BCO-DMO).
 818 (Version 1) Version Date 2023-07-19. doi:10.26008/1912/bco-dmo.904721.1
 819 Global Ocean Gridded L4 Sea Surface Heights And Derived Variables Reprocessed 1993-
 820 Ongoing. *E.U. Copernicus Marine Service Information (CMEMS). Marine Data Store*
 821 (*MDS*). DOI: [10.48670/moi-00148](https://doi.org/10.48670/moi-00148) (Accessed on 08-Aug-2023)
- 822 Haskell, W. Z., Fassbender, A. J., Long, J. S., & Plant, J. N. (2020). Annual Net Community
 823 Production of Particulate and Dissolved Organic Carbon From a Decade of Biogeochemical
 824 Profiling Float Observations in the Northeast Pacific. *Global Biogeochemical Cycles*, *34*(10),
 825 1–22. <https://doi.org/10.1029/2020GB006599>
- 826 Henson, S. A., Dunne, J. P., & Sarmiento, J. L. (2009). Decadal variability in North Atlantic
 827 phytoplankton blooms. *Journal of Geophysical Research: Oceans*, *114*(4), 1–11.
 828 <https://doi.org/10.1029/2008JC005139>
- 829 Henson, S. A., Robinson, I., Allen, J. T., & Waniek, J. J. (2006). Effect of meteorological
 830 conditions on interannual variability in timing and magnitude of the spring bloom in the
 831 Irminger Basin, North Atlantic. *Deep-Sea Research Part I: Oceanographic Research Papers*,
 832 *53*(10), 1601–1615. <https://doi.org/10.1016/j.dsr.2006.07.009>
- 833 Henson, S. A., Beaulieu, C., & Lampitt, R. (2016). Observing climate change trends in ocean
 834 biogeochemistry: When and where. *Global Change Biology*, *22*(4), 1561–1571.
 835 <https://doi.org/10.1111/gcb.13152>
- 836 Hersbach, H., Bell, B., Berrisford, P., Hirahara, S., Horányi, A., Muñoz-Sabater, J., Nicolas, J.,
 837 Peubey, C., Radu, R., Schepers, D., Simmons, A., Soci, C., Abdalla, S., Abellan, X.,
 838 Balsamo, G., Bechtold, P., Biavati, G., Bidlot, J., Bonavita, M., ... Thépaut, J. N. (2020). The
 839 ERA5 global reanalysis. *Quarterly Journal of the Royal Meteorological Society*, *146*(730),
 840 1999–2049. <https://doi.org/10.1002/qj.3803>
- 841 Hersbach, H., Bell, B., Berrisford, P., Biavati, G., Horányi, A., Muñoz Sabater, J., Nicolas, J.,
 842 Peubey, C., Radu, R., Rozum, I., Schepers, D., Simmons, A., Soci, C., Dee, D., Thépaut, J-N.
 843 (2023): ERA5 hourly data on single levels from 1940 to present. [Dataset]. Copernicus
 844 Climate Change Service (C3S) Climate Data Store (CDS),
 845 DOI: [10.24381/cds.adbb2d47](https://doi.org/10.24381/cds.adbb2d47) (Accessed on 13-Jul-2023)
- 846 Ho, D. T., Law, C. S., Smith, M. J., Schlosser, P., Harvey, M., & Hill, P. (2006). Measurements
 847 of air-sea gas exchange at high wind speeds in the Southern Ocean: Implications for global
 848 parameterizations. *Geophysical Research Letters*, *33*(16), 1–6.
 849 <https://doi.org/10.1029/2006GL026817>
- 850 Holte, J., Talley, L. D., Gilson, J., & Roemmich, D. (2017). An Argo mixed layer climatology
 851 and database. *Geophysical Research Letters*, *44*(11), 5618–5626.
 852 <https://doi.org/10.1002/2017GL073426>
- 853 Hopkins, J., Henson, S. A., Painter, S. C., Tyrrell, T., & Poulton, A. J. (2015). Phenological
 854 characteristics of global coccolithophore blooms. *Global Biogeochemical Cycles*, *29*(2), 239–
 855 253. <https://doi.org/10.1002/2014GB004919>
- 856 Huang, Y., Fassbender, A. J., Long, J. S., Johannessen, S., & Bif, M. B. (2022). Partitioning the
 857 Export of Distinct Biogenic Carbon Pools in the Northeast Pacific Ocean Using a
 858 Biogeochemical Profiling Float. *Global Biogeochemical Cycles*, *36*(2), 1–19.
 859 <https://doi.org/10.1029/2021GB007178>
- 860 Isern, A. R., & Clark, H. L. (2003). The Ocean Observatories Initiative: A Continued Presence
 861 for Interactive Ocean Research. *Marine Technology Society Journal*, *37*(3), 26–41.
 862 <http://www.neptune.washington.edu>

- 863 Jacobson, A. R., Schuldt, K. N., Arlyn Andrews, Miller, J. B., Oda, T., Sourish Basu, Mund, J.,
 864 Weir, B., Ott, L., Aalto, T., Abshire, J. B., Aikin, K., Aoki, S., Allen, G., Apadula, F.,
 865 Arnold, S., Baier, B., Bakwin, P., Bani, L., ... Miroslaw Zimnoch. (2023). *CarbonTracker*
 866 *CT-NRT.v2023-5*. NOAA Global Monitoring Laboratory. [https://doi.org/10.15138/FFXV-](https://doi.org/10.15138/FFXV-2Z26)
 867 [2Z26](https://doi.org/10.15138/FFXV-2Z26)
- 868 Jiang, Z. P., Hydes, D. J., Hartman, S. E., Hartman, M. C., Campbell, J. M., Johnson, B. D.,
 869 Schofield, B., Turk, D., Wallace, D., Burt, W. J., Thomas, H., Cosca, C., & Feely, R. (2014).
 870 Application and assessment of a membrane-based $p\text{CO}_2$ sensor under field and laboratory
 871 conditions. *Limnology and Oceanography: Methods*, *12*(APR), 264–280.
 872 <https://doi.org/10.4319/lom.2014.12.264>
- 873 Knor, L. A. C. M., Sabine, C. L., Sutton, A. J., White, A. E., Potemra, J., & Weller, R. A. (2023).
 874 Quantifying Net Community Production and Calcification at Station ALOHA Near Hawai'i:
 875 Insights and Limitations From a Dual Tracer Carbon Budget Approach. *Global*
 876 *Biogeochemical Cycles*, *37*(7), 1–22. <https://doi.org/10.1029/2022GB007672>
- 877 Kortzinger, A., Send, U., Lampitt, R. S., Hartman, S., Wallace, D. W. R., Karstensen, J.,
 878 Villagarcia, M. G., Llinás, O., & DeGrandpre, M. D. (2008). The seasonal $p\text{CO}_2$ cycle at
 879 $49^\circ\text{N}/16.5^\circ\text{W}$ in the northeastern Atlantic Ocean and what it tells us about biological
 880 productivity. *Journal of Geophysical Research*, *113*, 1–15.
 881 <https://doi.org/10.1029/2007JC004347>
- 882 Lacour, L., Briggs, N., Claustre, H., Ardyna, M., & Dall'Olmo, G. (2019). The Intraseasonal
 883 Dynamics of the Mixed Layer Pump in the Subpolar North Atlantic Ocean: A
 884 Biogeochemical-Argo Float Approach. *Global Biogeochemical Cycles*, *33*(3), 266–281.
 885 <https://doi.org/10.1029/2018GB005997>
- 886 Lai, C. Z., DeGrandpre, M. D., & Darlington, R. C. (2018). Autonomous optofluidic chemical
 887 analyzers for marine applications: Insights from the Submersible Autonomous Moored
 888 Instruments (SAMI) for pH and $p\text{CO}_2$. *Frontiers in Marine Science*, *4*(JAN), 1–11.
 889 <https://doi.org/10.3389/fmars.2017.00438>
- 890 Landschützer, P., Gruber, N., Bakker, D. C. E., Stemmler, I., & Six, K. D. (2018). Strengthening
 891 seasonal marine CO_2 variations due to increasing atmospheric CO_2 . *Nature Climate Change*,
 892 *8*(2), 146–150. <https://doi.org/10.1038/s41558-017-0057-x>
- 893 Landschützer, Peter; Laruelle, Goulven G.; Roobaert, Alizée; Regnier, Pierre (2020). A
 894 combined global ocean $p\text{CO}_2$ climatology combining open ocean and coastal areas (NCEI
 895 Accession 0209633). NOAA National Centers for Environmental Information. Dataset.
 896 <https://doi.org/10.25921/qb25-f418>. Accessed April 17, 2023.
- 897 Lauvset, S. K., Lange, N., Tanhua, T., Bittig, H. C., Olsen, A., Kozyr, A., Álvarez, M., Becker,
 898 S., Brown, P. J., Carter, B. R., Cotrim Da Cunha, L., Feely, R. A., Van Heuven, S.,
 899 Hoppema, M., Ishii, M., Jeansson, E., Jutterström, S., Jones, S. D., Karlsen, M. K., ... Key,
 900 R. M. (2021). An updated version of the global interior ocean biogeochemical data product,
 901 GLODAPv2.2021. *Earth System Science Data*, *13*(12), 5565–5589.
 902 <https://doi.org/10.5194/essd-13-5565-2021>
- 903 Lewis, E. R., & Wallace, D. W. R. (1998). Program Developed for CO_2 System Calculations. In
 904 *ESS-DIVE*. Environmental System Science Data Infrastructure for a Virtual Ecosystem.
 905 <https://doi.org/https://doi.org/10.15485/1464255>
- 906 Lueker, T. J., Dickson, A. G., & Keeling, C. D. (2000). Ocean $p\text{CO}_2$ calculated from dissolved
 907 inorganic carbon, alkalinity, and equations for K1 and K2: validation based on laboratory

- 908 measurements of CO₂ in gas and seawater at equilibrium. *Marine Chemistry*, 70(1–3), 105–
 909 119. [https://doi.org/10.1016/S0304-4203\(00\)00022-0](https://doi.org/10.1016/S0304-4203(00)00022-0)
- 910 Manning, C.C.M. and D.P. Nicholson (2022). dnicholson/gas_toolbox: MATLAB code for
 911 calculating gas fluxes. Zenodo. <https://doi.org/10.5281/zenodo.6126685>
- 912 Martin, P., Lampitt, R. S., Jane Perry, M., Sanders, R., Lee, C., & D’Asaro, E. (2011). Export
 913 and mesopelagic particle flux during a North Atlantic spring diatom bloom. *Deep-Sea*
 914 *Research Part I: Oceanographic Research Papers*, 58(4), 338–349.
 915 <https://doi.org/10.1016/j.dsr.2011.01.006>
- 916 McRaven, L. (2022a). Water temperature, salinity, and others taken by CTD and Niskin
 917 bottles from the research vessel Neil Armstrong in the North Atlantic Ocean during 2020
 918 Ocean Observations Initiative (OOI) Irminger Sea 7 and Overturning in the Subpolar North
 919 Atlantic Program – Greenland Deep Western Boundary Current, ONSAP-GDWBC, cruise
 920 AR46 from 2020-08-08 to 2020-08-26. (NCEI Accession 0252117) [Data set]. NOAA
 921 National Centers for Environmental Information. <https://doi.org/10.25921/51B4-AC30>
 922 <https://doi.org/10.25921/51b4-ac30>
- 923 McRaven, L. (2022b). Water temperature, salinity, and others taken by CTD and Niskin
 924 bottles from the research vessel Neil Armstrong, Irminger Sea 5 cruise AR30-03, in the
 925 North Atlantic from 2018-06-06 to 2018-06-22. (NCEI Accession 0252116) [Data set].
 926 NOAA National Centers for Environmental Information. [https://doi.org/10.25921/BFSV-](https://doi.org/10.25921/BFSV-YP35)
 927 <https://doi.org/10.25921/bfsv-yp35>
- 928 McRaven, L. (2022c). Water temperature, salinity, and others taken by CTD and Niskin
 929 bottles from the research vessel Neil Armstrong, cruise AR35-05, in the North Atlantic from
 930 08-02-2019 to 08-25-2019 (NCEI Accession 0251721) [Data set]. NOAA National Centers
 931 for Environmental Information. <https://doi.org/10.25921/61KN-QV10>
 932 <https://doi.org/10.25921/61kn-qv10>
- 933 McRaven, L. (2022d). Water temperature, salinity, and others taken by CTD and Niskin
 934 bottles from the research vessel Neil Armstrong, cruise AR60-01, in the North Atlantic from
 935 08-03-2021 to 08-17-2021 (NCEI Accession 0247461) [Data set]. NOAA National Centers
 936 for Environmental Information. <https://doi.org/10.25921/P8QE-ME08>
 937 <https://doi.org/10.25921/p8qe-me08>
- 938 Mignot, A., Ferrari, R., & Claustre, H. (2018). Floats with bio-optical sensors reveal what
 939 processes trigger the North Atlantic bloom. *Nature Communications*, 9(1).
 940 <https://doi.org/10.1038/s41467-017-02143-6>
- 941 Millero, F. J., Lee, K., & Roche, M. (1998). Distribution of alkalinity in the surface waters of the
 942 major oceans. *Marine Chemistry*, 60, 111–130.
- 943 *Ocean Observatories Initiative Science Prospectus: Scientific Objectives and Network Design*.
 944 (2007). https://io.ocean.washington.edu/files/science_prospectus_2007-10-10_lowres_0.pdf.
- 945 *OOI Data Product Specification for Water Temperature*. (2013).
 946 [https://oceanobservatories.org/wp-content/uploads/2023/09/1341-](https://oceanobservatories.org/wp-content/uploads/2023/09/1341-00130_Data_Product_Spec_TEMPSFL_OOI-2.pdf)
 947 [00130_Data_Product_Spec_TEMPSFL_OOI-2.pdf](https://oceanobservatories.org/wp-content/uploads/2023/09/1341-00130_Data_Product_Spec_TEMPSFL_OOI-2.pdf)
- 948 *OOI Data Product Specification for Salinity*. (2013). [https://oceanobservatories.org/wp-](https://oceanobservatories.org/wp-content/uploads/2015/10/1341-00040_Data_Product_SPEC_PRACSAL_OOI.pdf)
 949 [content/uploads/2015/10/1341-00040_Data_Product_SPEC_PRACSAL_OOI.pdf](https://oceanobservatories.org/wp-content/uploads/2015/10/1341-00040_Data_Product_SPEC_PRACSAL_OOI.pdf)
- 950 Olsen, A., Key, R. M., Van Heuven, S., Lauvset, S. K., Velo, A., Lin, X., Schirnick, C., Kozyr,
 951 A., Tanhua, T., Hoppema, M., Jutterström, S., Steinfeldt, R., Jeansson, E., Ishii, M., Pérez, F.
 952 F., & Suzuki, T. (2016). The global ocean data analysis project version 2 (GLODAPv2) - An

- 953 internally consistent data product for the world ocean. *Earth System Science Data*, 8(2), 297–
954 323. <https://doi.org/10.5194/essd-8-297-2016>
- 955 Orr, J. C., Epitalon, J. M., Dickson, A. G., & Gattuso, J. P. (2018). Routine uncertainty
956 propagation for the marine carbon dioxide system. *Marine Chemistry*, 207(October), 84–107.
957 <https://doi.org/10.1016/j.marchem.2018.10.006>
- 958 Painter, S. C., Henson, S. A., Forryan, A., Steigenberger, S., Klar, J., Stinchcombe, M. C.,
959 Rogan, N., Baker, A. R., Achterberg, E. P., & Moore, C. M. (2014). An assessment of the
960 vertical diffusive flux of iron and other nutrients to the surface waters of the subpolar North
961 Atlantic Ocean. *Biogeosciences*, 11(8), 2113–2130. <https://doi.org/10.5194/bg-11-2113-2014>
- 962 Palevsky, H. I., Clayton, S., Atamanchuk, D., Battisti, R., Batryn, J., Bourbonnais, A., Briggs, E.
963 M., Carvalho, F., Chase, A. P., Eveleth, R., Fatland, R., Fogaren, K. E., Fram, J. P., Hartman,
964 S. E., Le Bras, I., Manning, C. C. M., Needoba, J. A., Neely, M. B., Oliver, H., ... Wingard,
965 C. (2023). OOI Biogeochemical Sensor Data: Best Practices & User Guide. *The Global*
966 *Ocean Observing System*, 1.1.1, 1–135. <https://doi.org/10.25607/OBP-1865.2>
- 967 Palevsky, H. I., & Doney, S. C. (2018). How Choice of Depth Horizon Influences the Estimated
968 Spatial Patterns and Global Magnitude of Ocean Carbon Export Flux. *Geophysical Research*
969 *Letters*, 45(9), 4171–4179. <https://doi.org/10.1029/2017GL076498>
- 970 Palevsky, H. I., & Nicholson, D. P. (2018). The North Atlantic Biological Pump: Insights from
971 the Ocean Observatories Initiative Irminger Sea Array. *Oceanography*, 31(1), 42–49.
972 <https://doi.org/10.5670/oceanog.2018.108>
- 973 Palevsky, H. I., & Quay, P. D. (2017). Influence of biological carbon export on ocean carbon
974 uptake over the annual cycle across the North Pacific Ocean. *Global Biogeochemical Cycles*,
975 31(1), 81–95. <https://doi.org/10.1002/2016GB005527>
- 976 Palevsky, H. I., Fogaren, K. E., Nicholson, D. P., Yoder, M. (2023b) Supplementary discrete
977 sample measurements of dissolved oxygen, dissolved inorganic carbon, and total alkalinity
978 from Ocean Observatories Initiative (OOI) cruises to the Irminger Sea Array 2018-2019.
979 Biological and Chemical Oceanography Data Management Office (BCO-DMO). (Version 1)
980 Version Date 2023-07-19. doi:10.26008/1912/bco-dmo.904722.1
- 981 Quay, P., Emerson, S., & Palevsky, H. (2020). Regional Pattern of the Ocean's Biological Pump
982 Based on Geochemical Observations. *Geophysical Research Letters*, 47(14), 1–10.
983 <https://doi.org/10.1029/2020GL088098>
- 984 Quay, P., Stutsman, J., & Steinhoff, T. (2012). Primary production and carbon export rates
985 across the subpolar N. Atlantic Ocean basin based on triple oxygen isotope and dissolved O₂
986 and Ar gas measurements. *Global Biogeochemical Cycles*, 26(2), 1–13.
987 <https://doi.org/10.1029/2010GB004003>
- 988 Racapé, V., Pierre, C., Metzl, N., Lo Monaco, C., Reverdin, G., Olsen, A., Morin, P., Vázquez-
989 Rodríguez, M., Ríos, A. F., & Pérez, F. F. (2013). Anthropogenic carbon changes in the
990 Irminger Basin (1981-2006): Coupling $\delta^{13}\text{C}$ DIC and DIC observations. *Journal of Marine*
991 *Systems*, 126, 24–32. <https://doi.org/10.1016/j.jmarsys.2012.12.005>
- 992 Sanders, R., Henson, S. A., Koski, M., De La Rocha, C. L., Painter, S. C., Poulton, A. J., Riley,
993 J., Salihoglu, B., Visser, A., Yool, A., Bellerby, R., & Martin, A. P. (2014). The Biological
994 Carbon Pump in the North Atlantic. *Progress in Oceanography*, 129(PB), 200–218.
995 <https://doi.org/10.1016/j.pocean.2014.05.005>
- 996 Sathyendranath, S., Stuart, V., Nair, A., Oka, K., Nakane, T., Bouman, H., Forget, M. H., Maass,
997 H., & Platt, T. (2009). Carbon-to-chlorophyll ratio and growth rate of phytoplankton in the
998 sea. *Marine Ecology Progress Series*, 383, 73–84. <https://doi.org/10.3354/meps07998>

- 999 Sauv , J., Gray, A. R., Prend, C. J., Bushinsky, S. M., & Riser, S. C. (2023). Carbon Outgassing
1000 in the Antarctic Circumpolar Current Is Supported by Ekman Transport From the Sea Ice
1001 Zone in an Observation-Based Seasonal Mixed-Layer Budget. *Journal of Geophysical*
1002 *Research: Oceans*, 128(11). <https://doi.org/10.1029/2023JC019815>
- 1003 Siegel, D. A., DeVries, T., Cetini , I., & Bisson, K. M. (2023). Quantifying the Ocean’s
1004 Biological Pump and Its Carbon Cycle Impacts on Global Scales. *Annual Review of Marine*
1005 *Science*, 15, 329–356. <https://doi.org/10.1146/annurev-marine-040722>
- 1006 Smith, L. M., Barth, J. A., Kelley, D. S., Plueddemann, A., Rodero, I., Ulses, G. A., Vardaro, M.
1007 F., & Weller, R. (2018). The Ocean Observatories Initiative. *Oceanography*, 31(1), 16–35.
1008 <https://doi.org/10.5670/oceanog.2018.105>
- 1009 Stemmann, L., & Boss, E. (2012). Plankton and Particle size and Packaging: From Determining
1010 Optical Properties to Driving the Biological Pump. *Annual Review of Marine Science*, 4,
1011 263–290. <https://doi.org/10.1146/annurev-marine-120710-100853>
- 1012 Sterl, M. F., & de Jong, M. F. (2022). Restratification Structure and Processes in the Irminger
1013 Sea. *Journal of Geophysical Research: Oceans*, 127(12).
1014 <https://doi.org/10.1029/2022JC019126>
- 1015 Sverdrup, H. U. (1953). On conditions for the vernal blooming of phytoplankton. *J. Cons. Int.*
1016 *Explor. Mer.*, 18(3), 287-295.
- 1017 Takahashi, T., Sutherland, S. C., Sweeney, C., Poisson, A., Metzl, N., Tilbrook, B., Bates, N.,
1018 Wanninkhof, R., Feely, R. A., Sabine, C., Olafsson, J., & Nojiri, Y. (2002). Global sea–air
1019 CO₂ flux based on climatological surface ocean pCO₂, and seasonal biological and
1020 temperature effects. *Deep Sea Research Part II: Topical Studies in Oceanography*, 49, 1601–
1021 1622.
- 1022 Uppstr m, L. R. (1974). The boron/chlorinity ratio of deep-sea water from the Pacific Ocean.
1023 *Deep-Sea Research*, 21, 161–162. https://archive.org/details/sim_deep-sea-research_1974_21
- 1024 U.S. Integrated Ocean Observing System, 2020. QARTOD - Prospects for Real-Time Quality
1025 Control Manuals, How to Create Them, and a Vision for Advanced Implementation. 22 pp.
1026 DOI: 10.25923/ysj8-5n28
- 1027 V ge, K., Pickart, R. S., Moore, G. W. K., & Ribergaard, M. H. (2008). Winter mixed layer
1028 development in the central Irminger Sea: The effect of strong, intermittent wind events.
1029 *Journal of Physical Oceanography*, 38(3), 541–565. <https://doi.org/10.1175/2007JPO3678.1>
- 1030 Van Heuven, S., Pierrot, D., Rae, J. W. B., Lewis, E., & Wallace, D. W. R. (2011). MATLAB
1031 Program Developed for CO₂ System Calculations. ORNL/CDIAC-105b. [Software]. Carbon
1032 Dioxide Information Analysis Center (CDIAC). [https://doi.org/10.3334/CDIAC/OTG.](https://doi.org/10.3334/CDIAC/OTG.CO2SYS_MATLAB_V1.1)
1033 [CO2SYS_MATLAB_V1.1](https://doi.org/10.3334/CDIAC/OTG.CO2SYS_MATLAB_V1.1)
- 1034 Volk, T., & Hoffert, M. I. (1985). Ocean Carbon Pumps: Analysis of Relative Strength and
1035 Efficiencies in Ocean-Driven Atmospheric CO₂ Changes. *The Carbon Cycle and*
1036 *Atmospheric CO₂: Natural Variations Archean to Present*.
- 1037 Wanninkhof, R. (1992). Relationship between wind speed and gas exchange over the ocean.
1038 *Journal of Geophysical Research*, 97(C5), 7373–7382. <https://doi.org/10.1029/92JC00188>
- 1039 Wanninkhof, R. (2014). Relationship between wind speed and gas exchange over the ocean
1040 revisited. *Limnology and Oceanography: Methods*, 12(JUN), 351–362.
1041 <https://doi.org/10.4319/lom.2014.12.351>
- 1042 Weiss, R. F. (1974). Carbon Dioxide in water and seawater: The solubility of a non-ideal gas.
1043 *Marine Chemistry*, 2, 203–215. <https://doi.org/10.5194/bg-13-841-2016>

1044 Yang, B., Shadwick, E. H., Schultz, C., & Doney, S. C. (2021). Annual Mixed Layer Carbon
1045 Budget for the West Antarctic Peninsula Continental Shelf: Insights From Year-Round
1046 Mooring Measurements. *Journal of Geophysical Research: Oceans*, 126(4), 1–15.
1047 <https://doi.org/10.1029/2020JC016920>

1048

1049